Inorg. Chem. **2004**, *43*, 4154–4171

Supramolecular Spin-Crossover Iron Complexes Based on Imidazole–Imidazolate Hydrogen Bonds

Yukinari Sunatsuki,[†] Hiromi Ohta,[†] Masaaki Kojima,*[,†] Yuichi Ikuta,[‡] Yoshiyuki Goto,[‡] Naohide Matsumoto,[‡] Seiichiro Iijima,[§] Haruo Akashi,[||] Sumio Kaizaki,[⊥] Françoise Dahan,[⊗] and Jean-Pierre Tuchagues[⊗]

Department of Chemistry, Faculty of Science, Okayama University, Tsushima-naka 3-1-1, Okayama 700-8530, Japan, Department of Chemistry, Faculty of Science, Kumamoto University, Kurokami 2-39-1, Kumamoto 860-8555, Japan, National Institute of Advanced Industrial Science and Technology, Tsukuba 305-8566, Japan, Research Institute of Natural Sciences, Okayama University of Science, Ridai-cho, Okayama 700-0005, Japan, Department of Chemistry, Graduate School of Science, Osaka University, Toyonaka, Osaka 560-0043, Japan, and Laboratoire de Chimie de Coordination du CNRS, UPR 8241, 205 Route de Narbonne, 31077 Toulouse Cedex, France

Received February 9, 2004

The $[Fe^{II}(H_3L)](BF_4)_2 \cdot 3H_2O$ (**1**) complex was synthesized, where H_3L (tris{[2-{(imidazole-4-yl)methylidene}amino]-ethyl}amine) is a tripodal ligand obtained by condensation of tris(2-aminoethyl)amine and 4-formylimidazole (fim) in a 1:3 molar ratio. Starting from **1**, a series of complexes, $[Fe^{II}(H_{1.5}L)](BF_4)_{0.5}$ (**2**) (=$[Fe^{II}(H_3L)][Fe^{II}(L)]BF_4$), $[Fe(H_{1.5}L)]BF_4$ (**3**) (=$[Fe^{II}(H_3L)][Fe^{III}(L)](BF_4)_2$), $[Fe^{III}(H_3L)](BF_4)_3 \cdot fim \cdot H_2O$ (**4**), and $[Fe^{III}(L)] \cdot 2.5H_2O$ (**5**), has been synthesized and characterized. The single-crystal X-ray structure of each complex has been determined. The Fe^{II} compound, **2**, and a mixed valence Fe^{II}–Fe^{III} compound, **3**, involve formally hemi-deprotonated ligands, $H_{1.5}L$. The structure of **3** consists of a homochiral two-dimensional assembled sheet, arising from the intermolecular hydrogen bonds between $[Fe^{II}(H_3L)]^{2+}$ and $[Fe^{III}(L)]^0$ (**3**). All but **5** exhibit spin crossover between low-spin (LS) and high-spin (HS) states. This is a rare case where both Fe^{II} and Fe^{III} complexes containing the same ligand exhibit spin-crossover behavior. Magnetic susceptibility and Mössbauer studies showed that **3** has three accessible electronic states: LS Fe^{II}–LS Fe^{III}, HS Fe^{II}–LS Fe^{III}, and HS Fe^{II}–HS Fe^{III}. Compounds **1**–**3** show the light-induced excited spin-state trapping effect at the Fe^{II} sites upon irradiation with green light. The solution magnetic properties, electronic spectra, and electrochemical properties of **1**, **4**, and **5** were also studied.

Introduction

Increasing attention has been paid to bistable molecules because they can be used as molecular memories and switches in electronic devices.[1] Spin crossover (SCO) between the low-spin (LS) and high-spin (HS) states is observed in some octahedral $3d^n$ ($4 \leq n \leq 7$) metal complexes. SCO is the most spectacular example of molecular bistability and can be brought about by external perturbations such as temperature, light, pressure, and magnetic field.[2] Since the discovery of the light-induced excited spin-state trapping (LIESST) effect, photoswitchable SCO compounds with long-lived metastable states have become of interest.[2h,3] It is now well established that the elastic interaction between SCO sites within a crystal lattice is the predominant factor governing cooperativity and, consequently, bistability.[2g,4] From this viewpoint, two strategies are currently explored in the design of SCO compounds exhibiting strong intersite interactions, namely, the polymeric approach and the supramolecular approach. The former strategy consists of linking together the SCO sites by chemical bridges into polymeric structures.[1a,5] So far, one-dimensional (1D), two-dimensional (2D), and even three-

* Author to whom correspondence should be addressed. Fax: +81-86-251-7842. E-mail: kojima@cc.okayama-u.ac.jp.
[†] Okayama University.
[‡] Kumamoto University.
[§] National Institute of Advanced Industrial Science and Technology.
[||] Okayama University of Science.
[⊥] Osaka University.
[⊗] Laboratoire de Chimie de Coordination du CNRS Toulouse.

(1) (a) Kahn, O.; Martinez, J. C. *Science* **1998**, *279*, 44−48. (b) Irie, M. *Chem. Rev.* **2000**, *100*, 1685−1716. (c) Itkis, M. E.; Chi, X.; Cordes, A. W.; Haddon, R. C. *Science* **2002**, *296*, 1443−1445. (d) Irie, M.; Fukaminato, T.; Sasaki, T.; Tamai, N.; Kawai, T. *Nature* **2002**, *420*, 759−760. (e) Miller, J. S. *Angew. Chem., Int. Ed.* **2003**, *42*, 27−29.

10.1021/ic0498384 CCC: $27.50
Published on Web 06/18/2004

dimensional (3D) SCO compounds have been prepared, and their magnetic properties have been extensively investigated. The latter strategy consists of generating strong intermolecular interactions between mononuclear SCO sites through such interactions as hydrogen bonds[6] and $\pi-\pi$ stacking[4a,5a,7] to form supramolecular species. Novel ligand systems that would provide not only SCO behavior but also strong and extended elastic intersite interactions are still needed.

Here we report a supramolecular approach inducing strongly cooperative SCO behavior. Our strategy is based on the formation of an extended 2D-sheet structure, which arises from intermolecular hydrogen bonds. We have focused on metal complexes with a polydentate ligand involving imidazole groups,[8,9] because it is known that the imidazole group is a versatile complementary building component that can be used by both coordination bonds and hydrogen bonds for the construction of biologically relevant model compounds,[10] polynuclear cluster molecules,[11] and extended multidimensional architectures.[12] Recently, we have published a report on the homochiral 2D extended-network structure of $[Co^{III}(H_3L)][Co^{III}(L)]Cl_3 \cdot 8H_2O$, arising from intermolecular imidazole−imidazolate hydrogen bonds between $[Co^{III}(H_3L)]^{3+}$ and $[Co^{III}(L)]^0$, where H_3L denotes the tripodal hexadentate ligand derived from the 1:3 condensation of tris(2-aminoethyl)amine and 4-formylimidazole (Figure 1).[13] This formally hemi-deprotonated species, $[Co^{III}(H_{1.5}L)]Cl_{1.5} \cdot 4H_2O$ (i.e., $[Co^{III}(H_3L)][Co^{III}(L)]Cl_3 \cdot 8H_2O$), was prepared by controlled deprotonation of $[Co^{III}(H_3L)]Cl_3$ with a base. By using a similar procedure, we could obtain the SCO iron compounds $[Fe^{II}(H_{1.5}L)](BF_4)_{0.5}$ (**2**) (=$[Fe^{II}(H_3L)][Fe^{II}(L)]BF_4$) and $[Fe(H_{1.5}L)]BF_4$ (**3**) (=$[Fe^{II}(H_3L)][Fe^{III}(L)](BF_4)_2$), both having a 2D extended-network structure similar to that of $[Co^{III}(H_3L)][Co^{III}(L)]Cl_3 \cdot 8H_2O$. Compounds **2** and **3** are resolved spontaneously. We have studied the X-ray structures, Mössbauer spectra, magnetic properties, and the LIESST effect of the SCO homochiral 2D extended network structures **2** and **3**, together with those of the component or related compounds, $[Fe^{II}(H_3L)](BF_4)_2 \cdot 3H_2O$ (**1**), $[Fe^{III}(H_3L)](BF_4)_3 \cdot fim \cdot H_2O$ (**4**, fim = 4-formylimidazole), and $[Fe^{III}(L)] \cdot 2.5H_2O$ (**5**). Because the importance of noncoordinating counterions on the SCO behavior has been recognized in several compounds,[2g,14] we concentrate here on the tetrafluoroborate salts. Part of this work has been communicated previously.[15]

After this manuscript had been submitted, Brewer et al. reported structures and properties of several iron tripodal imidazole complexes, including $[Fe^{III}(L)] \cdot 3H_2O$.[16]

(2) (a) König, E. *Prog. Inorg. Chem.* **1987**, *35*, 527−623. (b) König, E. *Struct. Bonding* (*Berlin*) **1991**, *76*, 51. (c) Goodwin, H. A. *Coord. Chem. Rev.* **1976**, *18*, 293−325. (d) Gütlich, P.; Hauser, A.; Spiering, H. *Angew. Chem., Int. Ed. Engl.* **1994**, *33*, 2024−2054. (e) Real, J. A.; Gaspar, A. B.; Niel, V.; Muñoz, M. C. *Coord. Chem. Rev.* **2003**, *236*, 121−141. (f) Bousseksou, A.; Verelst, M.; Constant-Machado, H.; Lemercier, G.; Tuchagues, J.-P.; Varret, F. *Inorg. Chem.* **1996**, *35*, 110−115. (g) Lemercier, G.; Verelst, M.; Bousseksou, A.; Varret, F.; Tuchagues, J.-P. In *Magnetism: A Supramolecular Function*; Kahn, O., Ed.; NATO ASI Series, Series C 484; Kluwer Academic: Dordrecht, The Netherlands, 1996; pp 335−356. (h) Gütlich, P.; Garcia, Y.; Woike, T. *Coord. Chem. Rev.* **2001**, *219*−*221*, 839−879. (i) Bousseksou, A.; Nègre, N.; Goiran, M.; Salmon, L.; Boillot, M. L.; Boukhedaden, K.; Tuchagues, J.-P.; Varret, F. *Eur. Phys. J. B* **2000**, *13*, 451−456. (j) Nègre, N.; Consejo, C.; Goiran, M.; Bousseksou, A.; Varret, F.; Tuchagues, J.-P.; Barbaste, R.; Askénazy, S. *Physica B* **2001**, *294*−*295*, 91−95. (k) Goiran, M.; Consejo, C.; Boillot, M.-L.; Tuchagues, J.-P. *Phys. Rev. B: Condens. Matter Mater. Phys.* **2002**, *65*, 1727−1730. (l) Bousseksou, A.; Molnár, G.; Tuchagues, J.-P.; Menéndez, N.; Codjovi, E.; Varret, F. *C. R. Chimie* **2003**, *6*, 329−335.

(3) (a) Decurtins, S.; Gütlich, P.; Kohler, C. P.; Spiering, H.; Hauser, A. *Chem. Phys. Lett.* **1984**, *105*, 1−4. (b) Decurtins, S.; Gütlich, P.; Hasselbach, K. M.; Hauser, A.; Spiering, H. *Inorg. Chem.* **1985**, *24*, 2174−2178.

(4) (a) Hayami, S.; Gu, Z.-Z.; Shiro, M.; Einaga, Y.; Sato, O. *J. Am. Chem. Soc.* **2000**, *122*, 7126−7127. (b) Spiering, H.; Kohlhaas, T.; Romstedt, H.; Hauser, A.; Bruns-Yilmaz, C.; Kusz, J.; Gütlich, P. *Coord. Chem. Rev.* **1999**, *190*−*192*, 629−647. (c) Hauser, A.; Jeftic, J.; Romstedt, H.; Hinek, R.; Spiering, H. *Coord. Chem. Rev.* **1999**, *190*−*192*, 471−491.

(5) (a) Letard, J.-F.; Guionneau, P.; Rabardel, L.; Howard, J. A. K.; Goeta, A. E.; Chasseau, D.; Kahn, O. *Inorg. Chem.* **1998**, *37*, 4432−4441. (b) Garcia, Y.; Kahn, O.; Rabardel, L.; Chansou, B.; Salmon, L.; Tuchagues, J.-P. *Inorg. Chem.* **1999**, *38*, 4663−4670. (c) Breuning, E.; Ruben, M.; Lehn, J.-M.; Renz, F.; Garcia, Y.; Ksenofontov, V.; Gütlich, P.; Wegelius, E.; Rissanen, K. *Angew. Chem., Int. Ed.* **2000**, *39*, 2504−2507. (d) Moliner, N.; Muñoz, C.; Letard, S.; Solans, X.; Menendez, N.; Goujon, A.; Varret, F.; Real, J. A. *Inorg. Chem.* **2000**, *39*, 5390−5393. (e) Reger, D. L.; Little, C. A.; Rheingold, A. L.; Lam, M.; Liable-Sands, L. M.; Rhagitan, B.; Concolino, T.; Mohan, A.; Long, G. J.; Briois, V.; Grandjean, F. *Inorg. Chem.* **2001**, *40*, 1508−1520. (f) Vreugdenhil, W.; van Diemen, J. H.; de Graaff, R. A. G.; Haasnoot, J. G.; Reedijk, J.; van der Kraan, A. M.; Kahn, O.; Zarembowitch, J. *Polyhedron* **1990**, *9*, 2971−2979. (g) Ozarowski, A.; Shunzhong, Y.; McGarvey, B. R.; Mislankar, A.; Drake, J. E. *Inorg. Chem.* **1991**, *30*, 3167−3174. (h) Real, J. A.; Andres, E.; Muñoz, M. C.; Julve, M.; Granier, T.; Bousseksou, A.; Varret, F. *Science* **1995**, *268*, 265−267. (i) van Konningsbruggen, P. J.; Garcia, Y.; Kahn, O.; Fournes, L.; Kooijman, H.; Spek, A. L.; Haasnoot, J. G.; Moscovici, J.; Provost, K.; Michalowicz, A.; Renz, F.; Gütlich, P. *Inorg. Chem.* **2000**, *39*, 1891−1900. (j) Niel, V.; Thompson, A. L.; Muñoz, M. C.; Galet, A.; Goeta, A. E.; Real, J. *Angew. Chem., Int. Ed.* **2003**, *42*, 3760−3763. (k) Grunert, C. M.; Schweifer, J.; Weinberger, P.; Linert, W.; Mereiter, K.; Hilscher, G.; Wiesinger, G.; van Koningsbruggen, P. J. *Inorg. Chem.* **2004**, *43*, 155−165.

(6) (a) Sorai, M.; Ensling, J.; Hasselbach, K. M.; Gütlich, P. *Chem. Phys.* **1977**, *20*, 197−208. (b) Sugiyarto, K. H.; Weitzner, K.; Craig, D. C.; Goodwin, H. A. *Aust. J. Chem.* **1997**, *50*, 869−873.

(7) (a) Zhong, Z. J.; Tao, J.-Q.; Yu, Z.; Dun, C.-Y.; Liu, Y.-J.; You, X.-Z. *J. Chem. Soc., Dalton Trans.* **1998**, *26*, 327−328. (b) Létard, J.-F.; Guionneau, P.; Codjovi, E.; Lavastre, O.; Bravic, G.; Chasseau, D.; Kahn, O. *J. Am. Chem. Soc.* **1997**, *119*, 10861−10862.

(8) Miyasaka, H.; Okamura, S.; Nakashima, T.; Matsumoto, N. *Inorg. Chem.* **1997**, *36*, 4329−4335.

(9) (a) Mimura, M.; Matsuo, T.; Motoda, Y.; Matsumoto, N.; Nakashima, T.; Kojima, M. *Chem. Lett.* **1998**, 691−692. (b) Katsuki, I.; Matsumoto, N.; Kojima, M. *Inorg. Chem.* **2000**, *39*, 3350−3354. (c) Sunatsuki, Y.; Motoda, Y.; Matsumoto, N. *Coord. Chem. Rev.* **2002**, *226*, 199−209.

(10) (a) Kolks, G.; Frihart, C. R.; Rabinowitz, H. N.; Lippard, S. J. *J. Am. Chem. Soc.* **1976**, *98*, 5720−5721. (b) Lemercier, G.; Mulliez, E.; Brouca-Cabarrecq, C.; Dahan, F.; Tuchagues, J.-P. *Inorg. Chem.* **2004**, *43*, 2105−2113.

(11) Matsumoto, N.; Motoda, Y.; Matsuo, T.; Nakashima, T.; Re, N.; Dahan, F.; Tuchagues, J.-P. *Inorg. Chem.* **1999**, *38*, 1165−1173.

(12) Lorente, M. A. M.; Dahan, F.; Sanakis, Y.; Petrouleas, V.; Bousseksou, A.; Tuchagues, J.-P. *Inorg. Chem.* **1995**, *34*, 5346−5357.

(13) Katsuki, I.; Motoda, Y.; Sunatsuki, Y.; Matsumoto, N.; Nakashima, T.; Kojima, M. *J. Am. Chem. Soc.* **2002**, *124*, 629−640.

(14) (a) Renovitch, G. A.; Baker, W. A., Jr. *J. Am. Chem. Soc.* **1967**, *89*, 6377−6378. (b) Wiehl, L.; Kiel, G.; Köhler, C. P.; Spiering, H.; Gütlich, P. *Inorg. Chem.* **1986**, *25*, 1565−1571. (c) Köppen, H.; Müller, E. W.; Köhler, C. P.; Spiering, H.; Meissner, E.; Gütlich, P. *Chem. Phys. Lett.* **1982**, *91*, 348−352.

(15) (a) Sunatsuki, Y.; Ikuta, Y.; Matsumoto, N.; Ohta, H.; Kojima, M.; Iijima, S.; Hayami, S.; Maeda, Y.; Kaizaki, S.; Dahan, F.; Tuchagues, J.-P. *Angew. Chem., Int. Ed.* **2003**, *42*, 1614−1618. (b) Ohta, H.; Sunatsuki, Y.; Ikuta, Y.; Matsumoto, N.; Iijima, S.; Akashi, H.; Kambe, T.; Kojima, M. *Mater. Sci.* **2003**, *21*, 191−198. (c) Ohta, H.; Sunatsuki, Y.; Kojima, M.; Iijima, S.; Akashi, H.; Matsumoto, N. *Chem. Lett.* **2004**, *33*, 350−351.

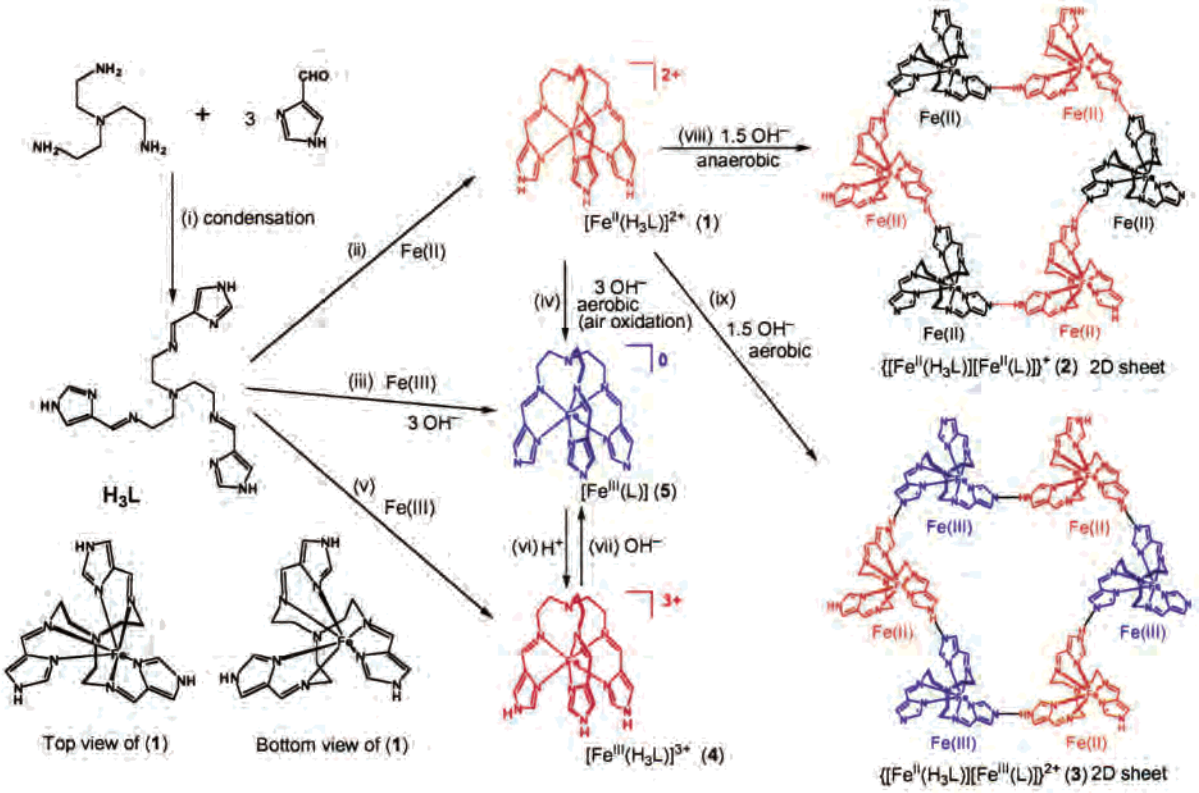

Figure 1. Synthetic procedures for the tripodal H_3L ligand and complexes **1**−**5**. (i) Condensation reaction of tris(2-aminoethyl)amine and 4-formylimidazole in a 1:3 molar ratio gave the tripodal ligand, H_3L. (ii) Reaction of H_3L with Fe^{II} yielded orange $[Fe^{II}(H_3L)]^{2+}$ (**1**). Top and bottom views of chiral complex **1** are shown bottom left of the figure. (iii) Reaction of H_3L with Fe^{III} in the presence of 3 equiv of a base yielded blue $[Fe^{III}(L)]^0$ (**5**). (iv) Complete deprotonation of **1** by the addition of 3 equiv of base in air also generated $[Fe^{III}(L)]^0$ (**5**). (v) The red Fe^{III} complex with the ligand in the neutral form, $[Fe^{III}(H_3L)]^{3+}$ (**4**), was prepared by the reaction of H_3L with Fe^{III}. (vi) Complete protonation of **5** by addition of an acid also generated complex **4**. (vii) Complete deprotonation of **4** by addition of a base gave **5**. (viii) Controlled deprotonation of the imidazole moieties of **1** upon addition of 1.5 equiv of base under anaerobic conditions yielded the hemi-deprotonated species, $[Fe^{II}(H_{1.5}L)]^{0.5+}$ (**2**) (=$\{[Fe^{II}(H_3L)][Fe^{II}(L)]\}^+$). Complex **2** has a homochiral 2D-sheet structure arising from the intermolecular imidazole−imidazolate hydrogen bonds between $[Fe^{II}(H_3L)]^{2+}$ and $[Fe^{II}(L)]^-$ with the same absolute configuration. (ix) When a reaction similar to (viii) was carried out under aerobic conditions, a dark green mixed-valence complex, $[Fe(H_{1.5}L)]^+$ (**3**) (=$\{[Fe^{II}(H_3L)][Fe^{III}(L)]\}^{2+}$), was obtained. Complex **3** also has a homochiral 2D-sheet structure. One of its components, $[Fe^{III}(L)]^0$, is generated by deprotonation and oxidation of **1**.

Results and Discussion

Synthesis and Characterization. The synthetic procedures yielding the tripodal H_3L ligand and complexes **1**−**5** are shown schematically in Figure 1. The tripodal H_3L ligand was prepared by reaction of tris(2-aminoethyl)amine and 4-formylimidazole in a 1:3 molar ratio in methanol. A solution containing this ligand was used for the synthesis of $[Fe^{II}(H_3L)](BF_4)_2\cdot 3H_2O$ (**1**). Complex **1** was obtained as orange crystals by mixing the ligand, $FeCl_2\cdot 4H_2O$, and NH_4BF_4 in a 1:1:3 molar ratio in the presence of a small amount of ascorbic acid to prevent air oxidation of Fe^{II} to Fe^{III}. Controlled deprotonation of the uncoordinated imidazole NH groups of **1** under *anaerobic conditions* yielded the hemi-deprotonated species $[Fe^{II}(H_{1.5}L)](BF_4)_{0.5}$ (**2**) (=$[Fe^{II}(H_3L)][Fe^{II}(L)]BF_4$). The reaction of **1** with NaOH or Et_3N in a 1:1 molar ratio under *aerobic conditions* yielded a dark green, mixed-valence complex, $[Fe(H_{1.5}L)]BF_4$ (**3**) (=$[Fe^{II}(H_3L)][Fe^{III}(L)](BF_4)_2$). Deprotonation induces oxidation of $[Fe^{II}(H_3L)]^{2+}$ to generate the $[Fe^{III}(L)]^0$ species, in which the ligand is deprotonated (L^{3-}) and which functions as a component of the mixed-valence complex, **3**. Thus, this reaction is an example of a proton-coupled electron-transfer reaction.[17] The dark red iron(III) complex with the tripodal ligand in its neutral form, $[Fe^{III}(H_3L)](BF_4)_3\cdot fim\cdot H_2O$ (**4**), was prepared similarly to **1**, except that $FeCl_3$ was used instead of $FeCl_2\cdot 4H_2O$, with water being used as the solvent. We could not obtain a fim-free iron(III) tetrafluoroborate complex in the crystalline state. The fully deprotonated blue iron(III) complex, $[Fe^{III}(L)]\cdot 2.5H_2O$ (**5**), was prepared by two methods: (i) by adding excess triethylamine to a methanol solution of $[Fe^{II}(H_3L)]^{2+}$ (**1**) under aerobic conditions, complex **1** being easily converted to **5** by deprotonation followed by air oxidation and (ii) by deprotonating $[Fe^{III}(H_3L)]^{3+}$ in water with aqueous NaOH, $[Fe^{III}(H_3L)]^{3+}$ being prepared in situ by reaction of $Fe^{III}Cl_3$ with H_3L.

The IR spectra of **1**−**5** were recorded at room temperature. All spectra showed strong characteristic absorptions around 1600 cm^{-1}, assignable to the C=N stretching vibration of the tripodal Schiff base ligand.[18] It has been shown that complexes with the ligand in the neutral form, H_3L, showed

(16) Brewer, C.; Brewer, G.; Marbury, G. S.; Viragh, C.; Beatty, A. M.; Scheidt, W. R. *Inorg. Chem.* **2004**, *43*, 2402−2415.

(17) (a) Slattery, S. J.; Blaho, J. K.; Lehnes, J.; Goldsby, K. A. *Coord. Chem. Rev.* **1998**, *174*, 391−416. (b) Carina, R. F.; Verzegnassi, L.; Bernardinelli, G.; Williams, A. F. *Chem. Commun.* **1998**, 2681−1682.

the ν(C=N) band in a higher wavenumber region ($\nu > 1610$ cm^{-1}) than those with the deprotonated L^{3-} form ($\nu < 1605$ cm^{-1}).[13,19,20] In fact, $[Fe^{II}(H_3L)](BF_4)_2 \cdot 3H_2O$ (**1**) and $[Fe^{III}(H_3L)](BF_4)_3 \cdot fim \cdot H_2O$ (**4**) show the ν(C=N) band at 1639 and 1623 cm^{-1}, respectively, while $[Fe^{III}(L)] \cdot 2.5H_2O$ (**5**) showed the band at a lower wavenumber (1590 cm^{-1}). Hemideprotonated complexes, **2** and **3**, show two ν(C=N) bands. The 1622 and 1594 cm^{-1} bands of **2** may be assigned to the C=N stretching vibration of $[Fe^{II}(H_3L)]^{2+}$ and $[Fe^{II}(L)]^{-}$, respectively. The presence of two component species with the ligand in its neutral form and in its deprotonated form has been confirmed in closely related complexes.[19,20] Complex **3** shows C=N stretching vibrations at 1634 and 1602 cm^{-1} at room temperature. They are attributable to the C=N stretching vibration of $[Fe^{II}(H_3L)]^{2+}$ and $[Fe^{III}(L)]^{0}$, respectively, and the presence of these two components was confirmed by X-ray crystallography. The C=N stretching vibration is sensitive not only to the nature of the ligand (neutral or deprotonated) but also to the spin-state of iron; a complex in the LS state shows the band at lower wavenumber than the HS complex. Thus, variable-temperature IR and Raman spectroscopy have been used to monitor the SCO behavior of related complexes.[21]

Solution Magnetic Susceptibility Data and Electronic Spectra. The solution magnetic susceptibilities of $[Fe^{II}(H_3L)](BF_4)_2 \cdot 3H_2O$ (**1**), $[Fe^{III}(H_3L)](BF_4)_3 \cdot fim \cdot H_2O$ (**4**), and $[Fe^{III}(L)] \cdot 2.5H_2O$ (**5**) were measured by the Evans method[22] at 297 K. The $\chi_M T$ value for **1** in CD_3OD (3.23 cm^3 K mol^{-1}) is in the range of values for HS Fe^{II}. The $\chi_M T$ values for **4** and **5** (3.63 and 0.67 cm^3 K mol^{-1}, respectively) are consistent with those for HS and LS Fe^{III} ions. All these results are in agreement with those of the variable-temperature magnetic susceptibility and Mössbauer studies for the solid samples (vide infra), although the SCO behavior in the solid state is influenced by such factors as the nature of the counteranion and the extent of solvation.[2d,5b,i,6] We have measured the solution magnetic susceptibility of $[Fe^{III}(L^{Me})] \cdot 3.5H_2O$ under the same conditions (H_3L^{Me} denotes the tripodal methyl derivative of H_3L, tris[2-(((2-methylimidazol-4-yl)methylidene)amino)ethyl]amine).[19] The $\chi_M T$ value for this complex of $(L^{Me})^{3-}$ was 1.6 cm^3 K mol^{-1} at 297 K in CD_3OD, which is intermediate between the spin-only values for HS and LS Fe^{III} (3:7 = HS/LS ratio evaluated on the basis of the spin-only values). Since $[Fe^{III}(L)] \cdot 2.5H_2O$ (**5**) is in the LS state under the same conditions, we may conclude that the methyl substitution at the 2-position of the imidazole moiety causes a slight decrease in the ligand-field strength.

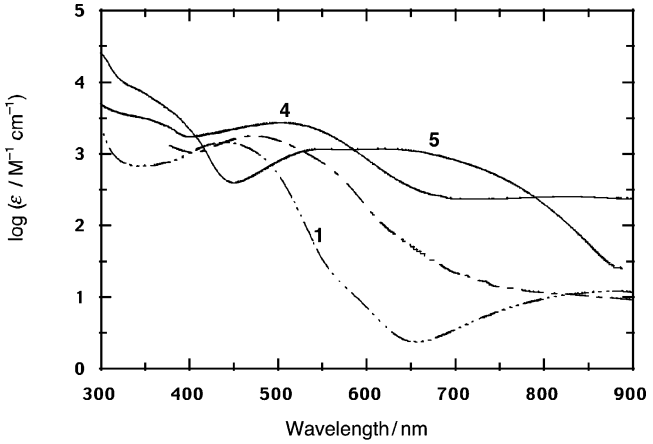

Figure 2. Electronic spectra of $[Fe^{II}(H_3L)]^{2+}$ (−···, **1**), $[Fe^{II}(L)]^{-}$ (−·−), $[Fe^{III}(H_3L)]^{3+}$ (—, **4**), and $[Fe^{III}(L)]$ (—, **5**) in methanol.

The electronic spectra of $[Fe^{II}(H_3L)]^{2+}$ (**1**), $[Fe^{II}(L)]^{-}$, $[Fe^{III}(H_3L)]^{3+}$ (**4**), and $[Fe^{III}(L)]^{0}$ (**5**), measured in methanol at ambient temperature, are shown in Figure 2. All complexes show intense charge-transfer (CT) bands ($\epsilon > 1000$ M^{-1} cm^{-1}) in the visible region, which tend to obscure weak d−d bands. The orange HS $[Fe^{II}(H_3L)]^{2+}$ (**1**) complex shows a metal-to-ligand charge-transfer (MLCT) band[23] at 441 nm ($\epsilon = 1430$ M^{-1} cm^{-1}) and a weak band in the near-infrared region ($\lambda_{max} = 881$ nm, $\epsilon = 12$ M^{-1} cm^{-1}), the latter being assigned to the spin-allowed $^5T_{2g} \rightarrow {}^5E_g(O_h)$ transition of the d^6 HS Fe^{II} state.[24] The reddish-orange $[Fe^{II}(L)]^{-}$ complex was prepared in situ by adding a methanol solution of NaOH to $[Fe^{II}(H_3L)]^{2+}$ in methanol under nitrogen because the complex is susceptible to oxidation. The d−d absorption bands of $[Fe^{II}(L)]^{-}$ are not clearly observed, probably because of the overlapping, intense CT transition, which is observed at a longer wavelength ($\lambda_{max} = 472$ nm, $\epsilon = 1760$ M^{-1} cm^{-1}) than for $[Fe^{II}(H_3L)]^{2+}$ ($\lambda_{max} = 441$ nm, $\epsilon = 1430$ M^{-1} cm^{-1}). The deprotonated ligand, L^{3-}, exhibits greater ligand-field strength than does the neutral ligand, H_3L. This is exemplified by the solution magnetic-susceptibility measurements: in CD_3OD at room temperature, $[Fe^{III}(L)]$ (**5**) is in the LS state, while $[Fe^{III}(H_3L)]^{3+}$ (**4**) is in the HS state. Thus, a bulge around 800 nm in the spectrum of $[Fe^{II}(L)]^{-}$ may be attributed to the $^5T_{2g} \rightarrow {}^5E_g(O_h)$ transition. Complex **4** shows an intense CT band in the visible region ($\lambda_{max} = 504$ nm, $\epsilon = 2690$ M^{-1} cm^{-1}) and a relatively weak band in the near-IR range ($\lambda_{max} = 830$ nm, $\epsilon = 252$ M^{-1} cm^{-1}). The LS complex, **5**, $[Fe^{III}(L)]$, exhibits two intense CT bands at 551 nm ($\epsilon = 1160$ M^{-1} cm^{-1}) and 617 nm ($\epsilon = 1170$ M^{-1} cm^{-1}), which probably hide weak d−d bands.

As we have reported in a previous paper,[19] with the addition of up to 3 equiv of NaOH, $[Fe^{II}(H_3L)]^{2+}$ (**1**) in

(18) Nakamoto, K. *Infrared and Raman Spectra of Inorganic and Coordination Compounds, Part B,* 5th ed.; John Wiley and Sons: New York, 1997.
(19) Ikuta, Y.; Ooidemizu, M.; Yamahata, Y.; Yamada, M.; Osa, S.; Matsumoto, N.; Iijima, S.; Sunatsuki, Y.; Kojima, M.; Dahan, F.; Tuchagues, J.-P. *Inorg. Chem.* **2003**, *42*, 7001−7017.
(20) Yamada, M.; Ooidemizu, I. Y. M.; Osa, S.; Matsumoto, N.; Iijima, S.; Kojima, M.; Dahan, F.; Tuchagues, J.-P. *Inorg. Chem.* **2003**, *42*, 8406−8416.
(21) (a) Herber, R. H.; Casson, L. M. *Inorg. Chem.* **1986**, *25*, 847−852. (b) Zilverentant, C. L.; van Albada, G. A.; Bousseksou, A.; Haasnoot, J. G.; Reedijk, J. *Inorg. Chim. Acta* **2000**, *303*, 287−290. (c) Sunatsuki, Y.; Sakata, M.; Matsuzaki, S.; Matsumoto, N.; Kojima, M. *Chem. Lett.* **2001**, 1254−1255.
(22) (a) Deutsch, J. L.; Poling, S. M. *J. Chem. Educ.* **1969**, *46*, 167−168. (b) Schubert, E. M. *J. Chem. Educ.* **1992**, *69*, 62.
(23) Levy, N. M.; Laranjeira, M. C.; Neves, A.; Franco, C. V. *J. Coord. Chem.* **1996**, *38*, 259−270.
(24) (a) Hayami, S.; Gu, Z.; Yoshiki, H.; Fujishima, A.; Sato, O. *J. Am. Chem. Soc.* **2001**, *123*, 11644−11650. (b) Boca, R.; Boca, M.; Dihan, L.; Falk, K.; Fuess, H.; Haase, W.; Jarosciak, R.; Papankova, B.; Renz, F.; Vrbova, M.; Werner, R. *Inorg. Chem.* **2001**, *40*, 3025−3033. (c) deVries, J. L. K. F.; Trooster, J. M.; de Bor, E. *J. Chem. Soc., Dalton Trans.* **1974**, 1771−1777.

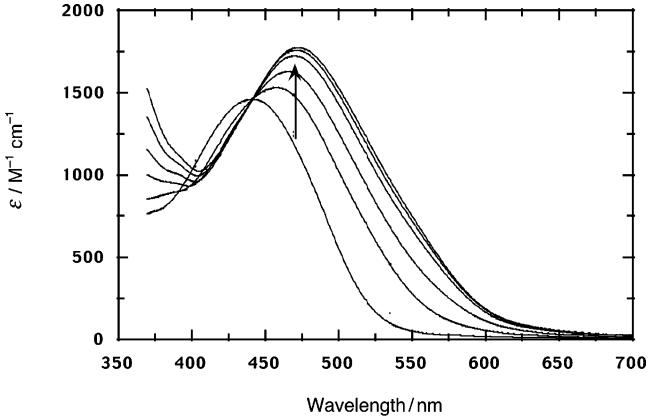

Figure 3. Electronic spectral changes of $[Fe^{II}(H_3L)]^{2+}$ (**1**) upon the addition of NaOH under nitrogen. To a methanol solution of **1** (0.30 mM) was added NaOH in methanol stepwise up to 3.0 equiv under nitrogen.

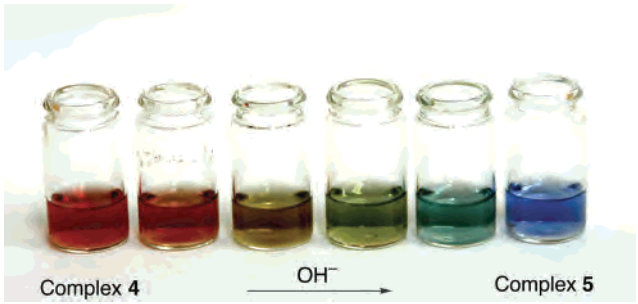

Figure 4. Color changes of $[Fe^{III}(H_3L)]^{3+}$ (**4**) in methanol by the addition of up to 3.1 equiv of NaOH in methanol.

methanol under aerobic conditions shows a drastic color change from yellowish-orange, through reddish-orange and green, to deep blue. Fe^{II} species are oxidized to Fe^{III} by air under basic conditions, and from the final blue solution, we obtained the iron(III) complex, **5**, $[Fe^{III}(L)]$, containing the deprotonated ligand, L^{3-}. Thus, the deprotonation reaction cannot be reversible. When the deprotonation reaction of **1** was carried out anaerobically, only a slight color change from yellowish-orange to reddish-orange was observed: aliquots of the methanolic NaOH solution were added, up to 3 equiv, to **1** in methanol, and the reaction was followed spectrophotometrically (Figure 3). No sharp isosbestic point was observed, probably because the pK_a values of $[Fe^{II}(H_nL)]^{(n-1)+}$ are similar to each other, and many species, $[Fe^{II}(H_3L)]^{2+}$, $[Fe^{II}(H_2L)]^{+}$, $[Fe^{II}(HL)]^{0}$, and $[Fe^{II}(L)]^{-}$, exist in equilibrium. The reaction is reversible: upon addition of $HClO_4$ in methanol to the resulting solution of $[Fe^{II}(L)]^{-}$ (reverse titration), the color changed from reddish-orange to yellowish-orange, and the spectrum of $[Fe^{II}(H_3L)]^{2+}$ (**1**) was regenerated.

The $[Fe^{III}(H_3L)]^{3+}$ complex, **4**, in methanol undergoes deprotonation upon addition of NaOH. The reaction is accompanied by impressive color changes from red, through brown and green, to blue (Figure 4), the spectral changes being shown in Figure 5. With the addition of up to 1.6 equiv of NaOH, a new band around 640 nm grows in intensity. On further addition of NaOH, the intensity of the band decreases, and two bands appear around 550 and 620 nm. The band at 504 nm decreases in intensity throughout the titration. The final spectrum is identical to the spectrum of

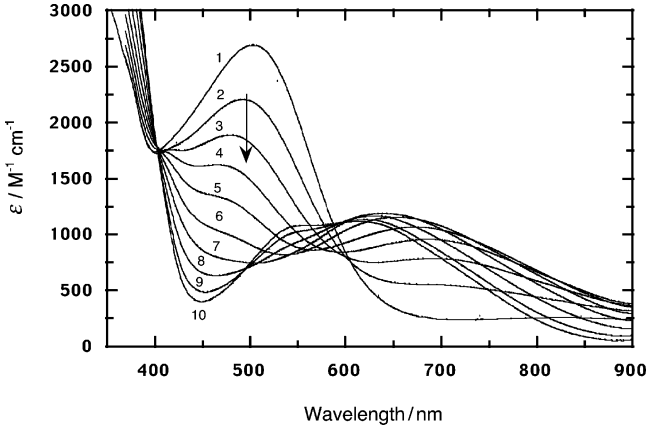

Figure 5. Electronic spectral changes of $[Fe^{III}(H_3L)]^{3+}$ (**4**) upon addition of NaOH. To a methanol solution of **4** (0.34 mM) was added NaOH in methanol, stepwise, up to 3.1 equiv: 1, 0; 2, 0.55; 3, 0.81; 4, 1.09; 5, 1.36; 6, 1.64; 7, 1.91; 8, 2.18; 9, 2.45; 10, 3.1 equiv. The color of the solution changed from red, through brown and green, to blue. The final spectrum (3.1 equiv of NaOH added) was identical to the spectrum of $[Fe^{III}(L)]$ (**5**).

$[Fe^{III}(L)]\cdot 2.5H_2O$ (**5**). Here again, no sharp isosbestic point was observed. The reaction is reversible: protonation of $[Fe^{III}(L)]$ in methanol takes place upon sequential addition of $HClO_4$ in methanol, and the complex is finally converted to $[Fe^{III}(H_3L)]^{3+}$.

Electrochemical Properties. The electrochemical properties of $[Fe^{II}(H_3L)](BF_4)_2\cdot 3H_2O$ (**1**), $[Fe^{III}(H_3L)](BF_4)_3\cdot fim\cdot H_2O$ (**4**), and $[Fe^{III}(L)]\cdot 2.5H_2O$ (**5**) were studied by cyclic voltammetry (CV). In methanol solution containing 0.1 M $LiClO_4$, the redox couple of **1** appears at -0.11 V ($E_{pc} = -0.15$ V, $E_{pa} = -0.08$ V) vs Ag/Ag^+ irrespective of the scan rate ($20 \le \nu \le 200$ mV s^{-1}), the peak current ratio i_p^a/i_p^c was found to be 1, (i_p^a or i_p^c)/$\nu^{1/2}$ was independent of ν, and the peak separation (ΔE_p) was 0.070 V (Supporting Information Figure 1). The corresponding iron(III) species, $[Fe^{III}(H_3L)](BF_4)_3\cdot fim\cdot H_2O$ (**4**), gave an identical CV under the same conditions. These results are consistent with an electrochemically reversible one-electron redox process (eq 1)

$$[Fe^{III}(H_3L)]^{3+} + e^- \rightleftharpoons [Fe^{II}(H_3L)]^{2+} \qquad (1)$$

The Fe^{III}/Fe^{II} redox couple for the Fe^{III} complex, **5**, $[Fe^{III}(L)]\cdot 2.5H_2O$, including the deprotonated ligand L^{3-}, is observed at -0.80 V vs Ag/Ag^+, and the couple is regarded as reversible based on the same criteria as above (Supporting Information Figure 1). Complete deprotonation of the ligand shifts the Fe^{III}/Fe^{II} redox potential to a more negative value from -0.11 to -0.80 V, i.e., 235 mV per proton. There is a strong coupling between electron and proton transfer: proton loss from the ligand is followed by electron loss from Fe^{II}. Deprotonation definitely favors the higher oxidation state, explaining the observation that $[Fe^{III}(L)]$ is easily formed upon deprotonation of $[Fe^{II}(H_3L)]^{2+}$ under aerobic conditions. Carina et al. reported that remote site deprotonation of a coordinated imidazole ligand switches the redox potential of coordinated iron by as much as 345 mV per proton.[17b]

As we have seen in the previous section, $[Fe^{III}(L)]$ (**5**) and $[Fe^{III}(H_3L)]^{3+}$ (**4**) in methanol undergo reversible protonation

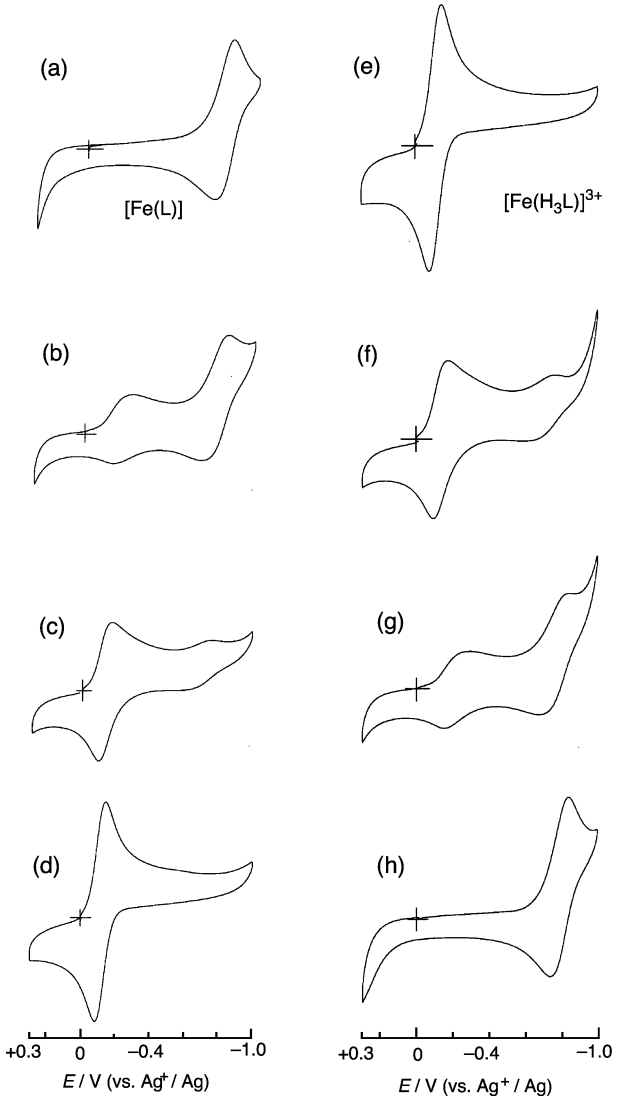

Figure 6. Progress of the protonation and deprotonation of $[Fe^{III}(L)]\cdot 2.5H_2O$ (**5**) and $[Fe^{III}(H_3L)](BF_4)_3\cdot fim\cdot H_2O$ (**4**) in methanol, respectively, as monitored by cyclic voltammetry. (a)−(d) Stepwise addition (0, 1, 2, and 3 equiv) of HCl in methanol to 1 mM $[Fe^{III}(L)]\cdot 2.5H_2O$ (**5**) in methanol. (e)−(h) Stepwise addition (0, 1, 2, and 3 equiv) of NaOMe in methanol to 1 mM $[Fe^{III}(H_3L)](BF_4)_3\cdot fim\cdot H_2O$ (**4**) in methanol.

or deprotonation upon addition of an acid or a base, respectively (protonation−deprotonation is associated with imidazole moieties). Figure 6 shows the progress of the reaction as monitored by cyclic voltammetry. Upon addition of 1 equiv of $HClO_4$ to $[Fe^{III}(L)]$ (**5**) in methanol (Figure 6b), the current intensity of the initial redox couple at −0.80 V ($E_p^c = -0.85$ V, $E_p^a = -0.75$ V; Figure 6a) diminishes and slightly shifts to a less negative potential ($E_p^c = -0.84$ V, $E_p^a = -0.68$ V), and a new redox couple appears at −0.22 V ($E_p^c = -0.27$ V, $E_p^a = -0.17$ V). The CV profile is independent of the sweep rate ($10 \le \upsilon \le 200$ mV s^{-1}). Upon addition of one more equivalent of HCl (Figure 6c), the second redox couple shifts to a less negative potential ($E_p^c = -0.18$ V, $E_p^a = -0.10$ V) and grows at the expense of the first redox couple, the initial redox couple shifting to a less negative potential ($E_p^c = -0.77$ V, $E_p^a = -0.60$ V). Full protonation at the imidazolate nitrogen moieties is achieved by adding 3 equiv of acid (Figure 6d), and the resulting CV is identical to that of $[Fe^{III}(H_3L)]^{3+}$ (**4**). A series of reverse reactions was observed when a base (NaOMe) was added to $[Fe^{III}(H_3L)]^{3+}$ (Figure 6e−h). These results are consistent with the acid−base equilibrium (eq 2) and consistent with those obtained by spectrophotometry.

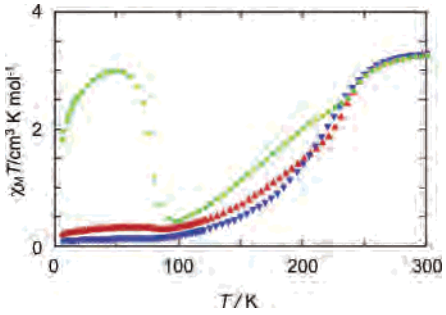

Figure 7. Magnetic behavior of $[Fe^{II}(H_3L)](BF_4)_2\cdot 3H_2O$ (**1**) in the form of $\chi_M T$ vs T plots. The sample was quickly cooled from 300 to 5 K and χ_M was successively measured in the warming (5−300 K, ▲) and cooling (300−5 K, ▼) modes, at a sweep rate of 2 K min^{-1}. The LIESST effect was observed by irradiation with green light ($\lambda_{max} = 500$ nm) at 5 K. After the light was switched off, the thermal dependence of $\chi_M T$ was recorded in the warming mode (●).

$$[Fe^{III}(L)] \underset{+H^+}{\overset{-H^+}{\rightleftharpoons}} [Fe^{III}(HL)]^+ \underset{+H^+}{\overset{-H^+}{\rightleftharpoons}} [Fe^{III}(H_2L)]^{2+} \underset{+H^+}{\overset{-H^+}{\rightleftharpoons}} [Fe^{III}(H_3L)]^{3+} \quad (2)$$

Analysis of the CVs, Figure 6a−h, suggests that each $[Fe^{III}(H_{3-n}L)]^{(3-n)+}$ ($n = 0-3$) species is characterized by a different position of the redox couple; as the degree of protonation increases, the redox potential becomes less negative (i.e., easier to reduce). It is worth noting that for a metal complex with a ligand exhibiting acid−base properties in aqueous solution, the redox potential value is pH dependent; usually, however, each species (fully deprotonated, mono-deprotonated, di-deprotonated, etc.) does not show an independent redox couple, but only an averaged couple is observed.[25,26] Studies in aqueous media were precluded for the present system because of the low solubility of $[Fe^{III}(L)]$ (**5**) and the instability of $[Fe^{III}(H_3L)](BF_4)_3$ (**4**).

Spin-Crossover Features of $[Fe^{II}(H_3L)](BF_4)_2\cdot 3H_2O$ (1) and of the Dehydrated Species. The magnetic behavior of **1** is shown in Figure 7 in the form of $\chi_M T$ versus T plots, where χ_M is the molar magnetic susceptibility and T is the absolute temperature. Complex **1** exhibits a gradual SCO behavior in the 110−270 K range. Complex **1** also exhibits the LIESST effect. Irradiation with green light ($\lambda_{max} = 500$ nm) at 5 K yields an increase in the $\chi_M T$ value, which is attributed to the LS to HS SCO at the Fe^{II} site. After the light source was switched off, the thermal dependence of the $\chi_M T$ value was recorded in the warming mode (2 K min^{-1}). The $\chi_M T$ value increased gradually and reached a maximum value of 3.02 cm^3 K mol^{-1} at 50 K. Above 50 K, the $\chi_M T$ value decreased, owing to thermal relaxation; the thermal relaxation was complete at 100 K. The reduced $\chi_M T$ value in the low-temperature range (<50 K) may result from

(25) Bond, A. M.; Haga, M. *Inorg. Chem.* **1986**, *25*, 4507−4514.
(26) Szulbinski, W.; Warburton, P. R.; Busch, D. H.; Alcock, N. W. *Inorg. Chem.* **1993**, *32*, 297−302.

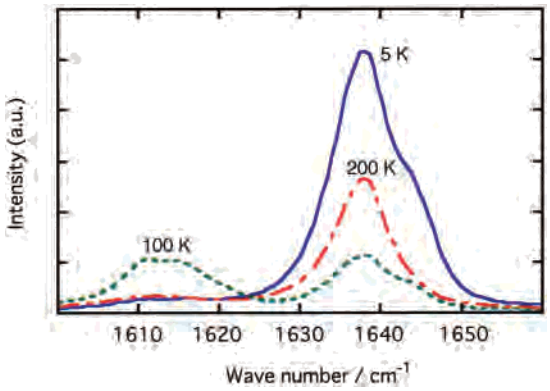

Figure 8. Variable-temperature (5−200 K) laser Raman spectra of [Fe^{II}(H$_3$L)](BF$_4$)$_2$·3H$_2$O (**1**) using an argon ion laser (λ = 514.5 nm) as the excitation radiation source: 5 K (—), 100 K (- - -), and 200 K (— - —). Compound **1** exhibits the LIESST effect at 5 K.

operation of zero-field splitting of the $S = 2$ ground state for the trapped HS molecules.

Variable-temperature laser Raman spectroscopy using an argon ion laser (λ = 514.5 nm) as the excitation radiation source also confirmed the LIESST effect.[27] The Raman spectra were measured in the 5−200 K temperature range, and the spin state at the Fe^{II} site was assigned on the basis of the characteristic band in the 1610−1640 cm^{-1} region due to the C═N stretching vibration of the Schiff-base ligand (Figure 8). At 200 K, the complex is mostly in the HS state, and it shows the C═N stretching band at 1638 cm^{-1}. As the temperature is lowered to 120 K, another C═N stretching band assignable to LS Fe^{II} appears at 1610 cm^{-1}, indicating SCO. However, below 100 K, the intensity of the band due to the HS species (1638 cm^{-1}) increases at the expense of the band due to the LS species (1610 cm^{-1}). At temperatures lower than 50 K, the predominant presence of the HS species is indicated. These results are ascribed to the transition from the LS to the HS state upon irradiation with an argon ion laser.

The SCO behavior of **1** was also studied using ^{57}Fe Mössbauer spectroscopy in the 78−298 K temperature range. Representative spectra are shown in Figure 9: at 78 K, the spectrum consisted of a single quadrupole-split doublet (δ = 0.42 mm s^{-1}, ΔE_Q = 0.20 mm s^{-1}), demonstrating the sole existence of LS Fe^{II}. At 180 and 220 K, an additional quadrupole-split doublet attributable to HS Fe^{II} was observed. No LS Fe^{II} was detected at 298 K. The HS Fe^{II} mole fraction in **1**, based on deconvolution analysis of the spectra, increases with increasing temperature: 0% (78 K), 23% (180 K), 44% (220 K), and 100% (298 K). These results are in agreement with the magnetic susceptibility results. When a sample of **1** was quenched at 78 K, the metastable HS state was frozen-in, and the Mössbauer spectrum showed a signal due to the presence of HS Fe^{II} (Figure 10a, δ = 1.15 mm s^{-1}, ΔE_Q = 2.13 mm s^{-1}) in an 8% mole fraction, in addition to the LS Fe^{II} species (δ = 0.43 mm s^{-1}, ΔE_Q = 0.20 mm s^{-1}). A frozen-in effect is observed when the relaxation rate is slow,

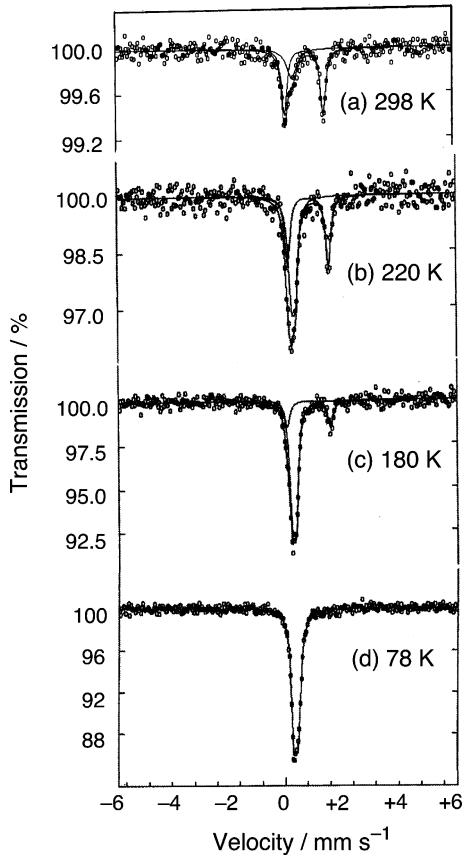

Figure 9. ^{57}Fe Mössbauer spectra of [Fe^{II}(H$_3$L)](BF$_4$)$_2$·3H$_2$O (**1**) at 298, 220, 180, and 78 K. The spectra shown were recorded in the heating mode after slow cooling of the sample from 295 to 78 K.

owing to cooperative interactions between SCO sites.[4] The Mössbauer spectra were also measured after **1** had been dried at 318 K in a vacuum of 10^{-5} mmHg. The resulting dehydrated [Fe^{II}(H$_3$L)](BF$_4$)$_2$ species did not show SCO but remained in the HS state over the entire 78−298 K temperature range (Figure 10c). This is an example of a material that becomes SCO inactive upon loss of the solvent molecules;[28,29] we discuss this in more detail below with regard to the crystal structure.

Spin-Crossover Features of [Fe^{II}(H$_{1.5}$L)](BF$_4$)$_{0.5}$ (2). We prepared **2** several times in the manner described in the Experimental Section, the samples being designated **2a**−**d**. We used **2a** for the X-ray structure analysis. Sample **2a** was left under ambient conditions for about 2 months, and this aged sample was named **2d**. Samples **2a**−**d** showed slightly different SCO behaviors from each other. The magnetic properties of **2a** are shown as a typical example in Supporting Information Figure 2 in the form of $\chi_M T$ versus T plots, where χ_M is the molar magnetic susceptibility per Fe and T is the absolute temperature. The magnetic behaviors of **2a** in the warming and cooling modes were very similar to each other and exhibited only a small thermal hysteresis in the SCO

(27) Suemura, N.; Ohama, M.; Kaizaki, S. *Chem. Commun.* **2001**, 1538−1539.

(28) (a) van Koningsbruggen, P. J.; Garcia, Y.; Kooijman, H.; Spek, A. L.; Haasnoot, J. G.; Kahn, O.; Linares, J.; Codjovi, E.; Varret, F. *J. Chem. Soc., Dalton Trans.* **2001**, 466−471. (b) Halder, G. J.; Kepert, C. J.; Moubaraki, B.; Murray, K. S.; Cashion, J. D. *Science* **2002**, *29*, 1762−1765. (c) Kröber, J.; Codjovi, E.; Kahn, O.; Groliere, F.; Jay, C. *J. Am. Chem. Soc.* **1993**, *115*, 9810−9811.

(29) Sorai, M. *Bull. Chem. Soc. Jpn.* **2001**, *74*, 2223−2253.

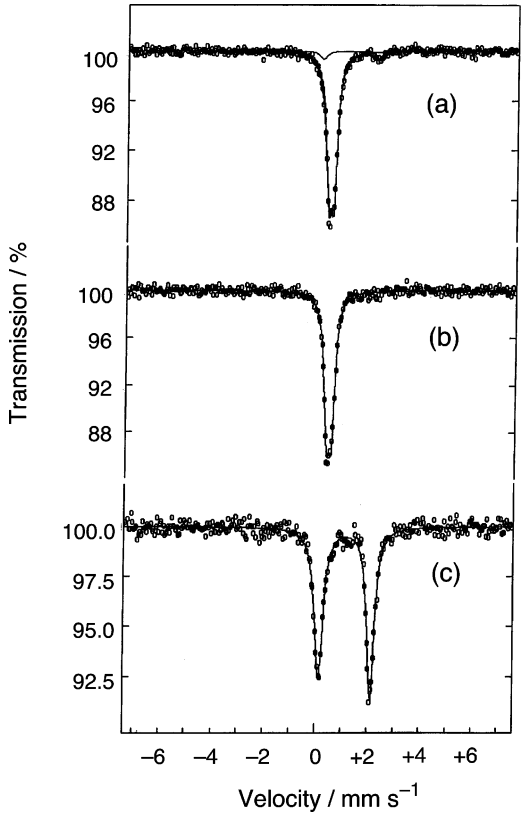

Figure 10. ^{57}Fe Mössbauer spectra of $[Fe^{II}(H_3L)](BF_4)_2 \cdot 3H_2O$ (**1**) at 78 K (a) after rapid cooling, and (b) after gradual cooling, and (c) the ^{57}Fe Mössbauer spectrum of dehydrated $[Fe^{II}(H_3L)](BF_4)_2$ at 78 K after rapid cooling.

region. The behavior in the cooling mode is described hereafter. The $\chi_M T$ value for **2a** at 300 K (1.78 cm^3 K mol^{-1}) is intermediate between the spin-only values of 3.0 cm^3 K mol^{-1} for HS Fe^{II} ($S = 4/2$, $g = 2.00$) and 0 cm^3 K mol^{-1} for LS Fe^{II} ($S = 0$, $g = 2.00$). The observed value is rather close to what is expected for a 1:1 mixture of LS Fe^{II} and HS Fe^{II}. On cooling, the $\chi_M T$ value gradually decreased, and at 190 K, it reached 0 cm^3 K mol^{-1}, the value expected for LS Fe^{II}. These results are consistent with the crystallographic results (vide infra). That **2** (=$[Fe^{II}(H_3L)][Fe^{II}(L)]BF_4$) exhibits SCO at a higher temperature than **1** (=$[Fe^{II}(H_3L)](BF_4)_2 \cdot 3H_2O$) indicates that **2** has a larger ligand-field strength than **1**. This result is in agreement with our observation that the ligand-field strength increases upon deprotonation of $[Fe^{II}(H_3L)]^{2+}$ and $[Fe^{III}(H_3L)]^{3+}$. Compound **2a** showed the LIESST effect. Irradiation with green light ($\lambda = 532$ nm) at 5 K yielded a drastic increase in the $\chi_M T$ value due to LS → HS conversion. After the light source was switched off, the thermal dependence of the $\chi_M T$ value was recorded in the warming mode (2 K min^{-1}). The $\chi_M T$ value increased gradually and reached a maximum at 50 K. Above 50 K, the $\chi_M T$ value decreased, owing to thermal relaxation; the thermal relaxation was complete at 100 K.

The SCO of **2** was also studied by ^{57}Fe Mössbauer spectroscopy in the 78−298 K range. Figure 11 shows the Mössbauer spectra of **2a** at 78, 240, 260, and 298 K. The Mössbauer parameters for **2b**−**d** are listed in Supporting Information Table 1. The Mössbauer spectra showed that,

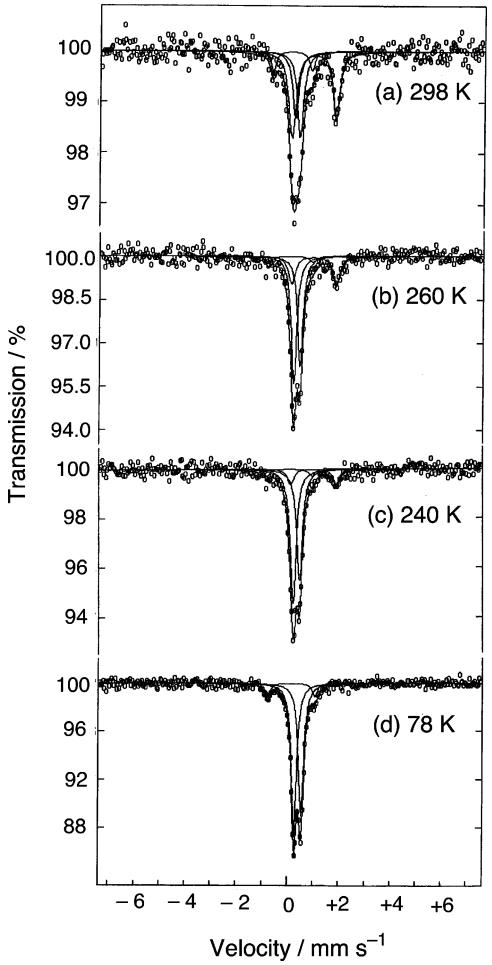

Figure 11. ^{57}Fe Mössbauer spectra of $[Fe^{II}(H_{1.5}L)](BF_4)_{0.5}$ (**2a**) at (a) 298 K, (b) 260 K, (c) 240 K, and (d) 78 K. The spectra shown were recorded in the heating mode after rapid cooling of the sample from 295 to 78 K.

Table 1. Temperature Dependence of the High-Spin Fe(II) Molar Fraction for $[Fe^{II}(H_{1.5}L)](BF_4)_{0.5}$ (**2a**−**d**)

		HS Fe^{II} (%)				
sample	Fe^{III} (%)	78 K	200 K	240 K	260 K	298 K
2a	8	0	0	12	23	42
2b	16	0	21	35		
2c	17	0			42	55
2d	36	8				82

despite the use of ascorbic acid as a reducing agent in the preparation, the samples were contaminated with LS Fe^{III} to different degrees (**2a**, 8%; **2b**, 16%; **2c**, 17%; **2d**, 36%). It is to be noted that **2d** is an aged sample of **2a**. The Mössbauer results suggest that **2** is easily oxidized, even in the solid state. The HS Fe^{II} mole fraction increases with temperature: for **2a**, 0% (78 K, 200 K), 12% (240 K), 23% (260 K), and 42% (298 K). Spectra for other samples, **2b**−**d**, were treated similarly. The HS Fe^{II} fractions for all samples at each temperature are compared in Table 1. Interestingly, there is an obvious correlation between the Fe^{III} mole fraction and the HS Fe^{II} fraction: the higher the mole fraction of Fe^{III}, the higher the HS fraction of Fe^{II} at a given temperature. This observation indicates that samples **2a**−**d** are not a mixture of, for example, $[Fe^{II}(H_3L)][Fe^{II}(L)]BF_4$ and $[Fe^{II}(H_3L)][Fe^{III}(L)](BF_4)_2$ but a nonstoichiometric compound formulated as $\{[Fe^{II}(H_3L)][Fe^{II}(L)]\}_{1-x}[Fe^{III}(L)]_x(BF_4)_{1+x}$.

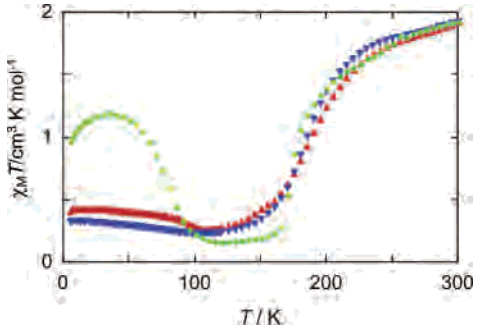

Figure 12. Magnetic behavior of $[Fe(H_{1.5}L)]BF_4$ (**3**) (=$[Fe^{II}(H_3L)][Fe^{III}(L)](BF_4)_2$) in the form of $\chi_M T$ vs T plots. The sample was cooled quickly from 300 to 5 K, and χ_M was measured in the warming (▲) and cooling (▼) modes. A further 5−350 K warming and cooling cycle yielded similar results to that of the first cooling mode. The LIESST effect was observed by irradiation with green light (λ_{max} = 500 nm) at 5 K. After the light was switched off, the thermal dependence of $\chi_M T$ was recorded in the warming mode (●).

Spin-Crossover Features of $[Fe(H_{1.5}L)]BF_4$ (3). The magnetic behavior of the mixed-valence complex, $[Fe(H_{1.5}L)]BF_4$ (**3**) (=$[Fe^{II}(H_3L)][Fe^{III}(L)](BF_4)_2$), is shown in Figure 12 in the form of $\chi_M T$ versus T plots, where χ_M is the molar magnetic susceptibility per Fe and T is the absolute temperature. The sample was quickly cooled from 300 to 5 K, and χ_M was successively measured in the warming (5 → 350 K) and cooling (350 → 5 K) modes, and then the cycle (5 → 350 → 5 K) was repeated. In the second cycle, the magnetic behaviors are the same as that of the cooling mode in the first cycle. The SCO was rather gradual in the first warming mode, and the result was different from the others, probably because of the frozen-in effect. The behavior for the warming mode in the second cycle is described hereafter. In the 5−150 K temperature range, $\chi_M T$ = 0.2 cm^3 K mol^{-1}, which is in the range expected for LS states at both the Fe^{II} (S = 0) and Fe^{III} (S = 1/2) sites. The $\chi_M T$ value changes rather abruptly in the 180−200 K range, indicating SCO at the Fe^{II} site. The $\chi_M T$ value at 200 K (1.8 cm^3 K mol^{-1}) is close to the calculated value for HS Fe^{II} (S = 2) and LS Fe^{III} ($\chi_M T$ = 1.69 cm^3 K mol^{-1}). Above 200 K, the $\chi_M T$ value increases gradually, owing to SCO from LS to HS Fe^{III}. The value of $\chi_M T$ = 2.22 cm^3 K mol^{-1} at 300 K is close to the calculated value ($\chi_M T$ = 2.36 cm^3 K mol^{-1}) for HS Fe^{II} and a 2:1 mixture of LS and HS Fe^{III}, as determined by X-ray crystallography (vide infra). We conclude that **3** undergoes SCO between three accessible electronic states: LS Fe^{II}−LS Fe^{III} ⇄ HS Fe^{II}−LS Fe^{III} ⇄ HS Fe^{II}−HS Fe^{III}. This complex also shows the LIESST effect (Figure 12). Irradiation with green light (λ_{max} = 500 nm) at 5 K yields an increase in the $\chi_M T$ value, attributable to the LS to HS SCO at the Fe^{II} site. After the light was switched off, the HS Fe^{II} state is retained at 5 K; on warming, the thermal relaxation was complete above 100 K.

The SCO of **3** was also studied by ^{57}Fe Mössbauer spectroscopy in the 78−309 K range. The sample was initially rapidly cooled to 78 K, and the spectra were measured at selected temperatures in the warming mode and then in the cooling mode. The spectra obtained in the two modes are nearly the same. Representative spectra are shown in Figure 13 and the data are listed in Supporting Information Table 2. At 78 K, the Mössbauer spectrum consisted of two quadrupole-split doublets (LS Fe^{III}, δ = 0.19 mm s^{-1}, ΔE_Q = 1.84 mm s^{-1}; LS Fe^{II}, δ = 0.42 mm s^{-1}, ΔE_Q = 0.32 mm s^{-1}), demonstrating that both the Fe^{II} and Fe^{III} sites were in the LS state. In the 150−210 K temperature range, three doublets were superimposed, owing to the coexistence of LS and HS Fe^{II} sites and LS Fe^{III} sites. As the temperature rose in the 150−210 K range, the intensity of the HS Fe^{II} absorption increased at the expense of the LS Fe^{II} absorption. At 250 K, essentially only two doublets due to HS Fe^{II} and LS Fe^{III} were observed. At 298 K, an absorption due to HS Fe^{III} was observed in addition to the absorptions of HS Fe^{II} and LS Fe^{III}. The HS Fe^{II} mole fraction vs T plots obtained by deconvolution analyses of the Mössbauer spectra are shown in Figure 14. The values obtained in the heating and cooling modes were the same within experimental error. The Mössbauer and magnetic susceptibility results are in agreement.

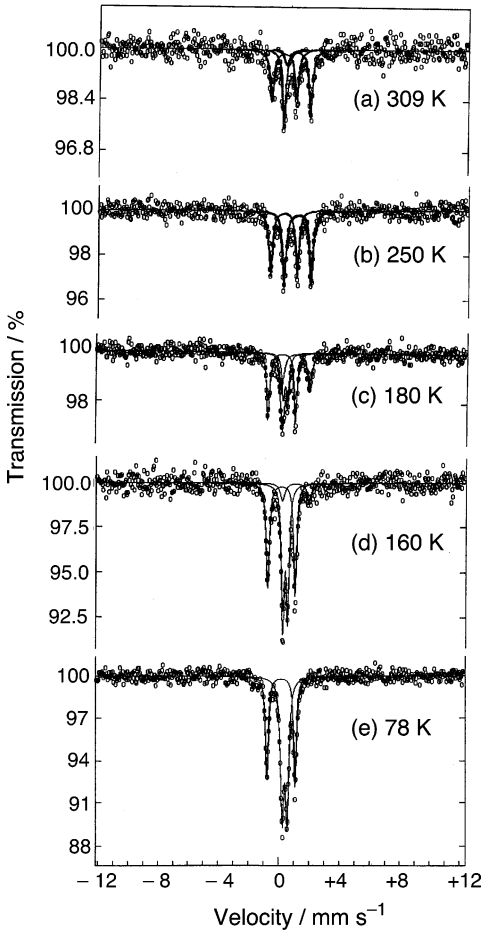

Figure 13. ^{57}Fe Mössbauer spectra of $[Fe(H_{1.5}L)]BF_4$ (**3**) (= $[Fe^{II}(H_3L)][Fe^{III}(L)](BF_4)_2$) at (a) 309 K, (b) 250 K, (c) 180 K, (d) 160 K, and (e) 78 K. The spectra shown were recorded in the heating mode after rapid cooling of the sample from 295 to 78 K.

Spin-Crossover Features of $[Fe^{III}(H_3L)](BF_4)_3 \cdot fim \cdot H_2O$ (4) and $[Fe^{III}(L)] \cdot 2.5H_2O$ (5). The temperature dependence (5−300 K) of the magnetic susceptibility indicated a SCO behavior for **4**.[15c] The result is shown in Figure 15 in the form of $\chi_M T$ versus T plots. The $\chi_M T$ value of **4** in the 5−150 K range is nearly constant at 0.58 cm^3 K mol^{-1}, indicating

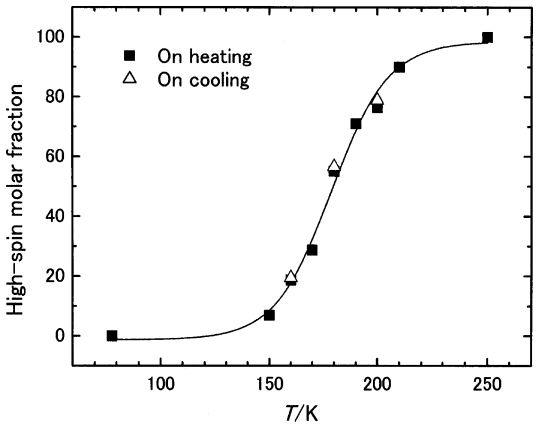

Figure 14. Mole fraction of the HS Fe^{II} sites vs T plots obtained by deconvolution analyses of the Mössbauer spectra of $[Fe(H_{1.5}L)]BF_4$ (**3**) (=$[Fe^{II}(H_3L)][Fe^{III}(L)](BF_4)_2$). The ■ values were obtained from the spectra recorded upon heating the sample after rapid cooling to 78 K, and the △ values were obtained from the spectra on subsequent cooling.

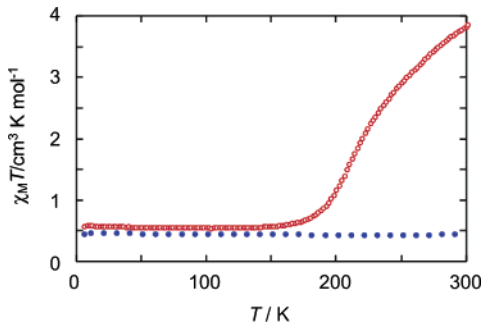

Figure 15. Magnetic behaviors of $[Fe^{III}(H_3L)](BF_4)_3$·fim·H_2O (**4**, ○) and $[Fe^{III}(L)]$·$2.5H_2O$ (**5**, ●) in the form of $\chi_M T$ vs T plots.

that Fe^{III} is in the LS state in this temperature range. In the 150−300 K range, the $\chi_M T$ value increases with increasing temperature from 0.60 cm^3 K mol^{-1} at 150 K to 3.88 cm^3 K mol^{-1} at 300 K. The $\chi_M T$ value at 300 K is lower than the spin-only value of 4.375 cm^3 K mol^{-1} for HS Fe^{III} ($S = 5/2$, $g = 2.00$). This fact indicates that complex **4** is not completely in the HS state at 300 K but contains LS sites (ca. 13%).

The SCO behavior of **4** was also studied by ^{57}Fe Mössbauer spectroscopy. The spectra were measured at 78, 200, 240, and 298 K: they are shown in Figure 16 and the data are listed in Supporting Information Table 3. At 78 K, the spectrum consisted of a single doublet, demonstrating the sole existence of LS Fe^{III}. At 200 and 240 K, in addition to the LS Fe^{III} doublet, a signal assignable to HS Fe^{III} was observed. The HS Fe^{III} mole fraction increased with temperature: 0% (78 K), 16% (200 K), and 45% (240 K). These results agree well with the magnetic susceptibility results. At 298 K, the spectrum was extremely broadened. An averaged line shape is observed when the rate of spin-state conversion between LS and HS Fe^{III} is comparable with, or faster than, the time scale of the Mössbauer experiment (ca. 10^7 s^{-1}).[30]

At this point, it is worth mentioning that it is rare that both Fe^{II} and Fe^{III} complexes with the same ligand exhibit

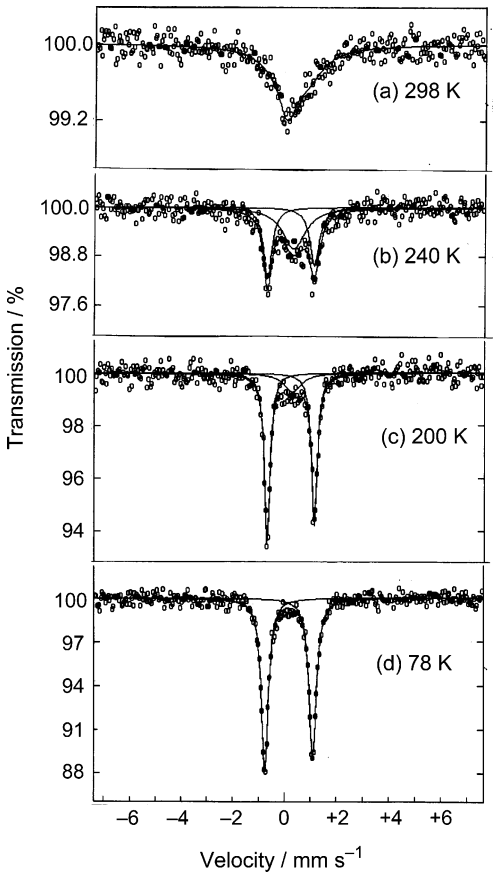

Figure 16. ^{57}Fe Mössbauer spectra of $[Fe^{III}(H_3L)](BF_4)_3$·fim·H_2O (**4**) at (a) 298 K, (b) 240 K, (c) 200 K, and (d) 78 K. The spectra shown were recorded in the heating mode after rapid cooling of the sample from 295 to 78 K.

SCO. In general, the oxidation state of a metal ion has a large effect on the SCO behavior. Thus, a larger ligand-field strength characterizes the Fe^{III}, compared with the corresponding Fe^{II} complex, and one does not expect SCO for both Fe^{III} and Fe^{II} complexes with the same ligand. We have shown in this paper that both Fe^{II} and Fe^{III} complexes of the H_3L ligand, **1** and **4**, show SCO behavior. To the best of our knowledge, only two ligands (1,1′,4,4′,5,5′,6,6′-octahydro-2,2′-bipyrimidine and 1,10-bis(5-nitrosalicylideneimine)-4,7-aminodecane) have been reported to generate SCO conditions for both Fe^{II} and Fe^{III} complexes.[31] The X-ray structures of the corresponding iron complexes have not been determined, except for $[Fe^{II}$(1,10-bis(5-nitrosalicylideneimine)-4,7-aminodecane)].[31d] The Fe^{III} complex with the deprotonated ligand, $[Fe^{III}(L)]$·$2.5H_2O$ (**5**), remains in the LS state over the 5−300 K range (Figure 15). Recently, we have reported that the corresponding methyl substituted complex, $[Fe^{III}(L^{Me})]$·$3.5H_2O$, exhibits SCO behavior.[19] The magnetic susceptibility results for the solid samples are in agreement with those previously described for solutions.

(30) Maeda, Y.; Tsutsumi, N.; Takashima, Y. *Inorg. Chem.* **1984**, *23*, 2440−2447.

(31) (a) Burnett, M. G.; McKee, V.; Nelson, S. M. *J. Chem. Soc., Dalton Trans.* **1981**, *9*, 1492−1497. (b) Tweedle, M. F.; Wilson, L. J. *J. Am. Chem. Soc.* **1976**, *98*, 4824−4834. (c) Petrouleas, V.; Tuchagues, J. P. *Chem. Phys. Lett.* **1987**, *137*, 21−25. (d) Boinnard, D.; Bousseksou, A.; Dworkin, A.; Savariault, J.-M.; Varret, F.; Tuchagues, J.-P. *Inorg. Chem.* **1994**, *33*, 271−281.

Table 2. Crystallographic Data for $[Fe^{II}(H_3L)](BF_4)_2 \cdot 3H_2O$ (**1**) and $[Fe^{II}(H_{1.5}L)](BF_4)_{0.5}$ (**2**) (=$[Fe^{II}(H_3L)][Fe^{II}(L)]BF_4$)

	1		**2**	
formula	$C_{18}H_{30}B_2F_8\,FeN_{10}O_3$		$C_{18}H_{22.5}B_{0.5}\,F_2N_{10}Fe$	
T (K)	293	108	293	93
mol wt	663.95	663.95	478.19	478.19
crystal system	trigonal	trigonal	trigonal	trigonal
space group	$R32(h)$ (No. 155)	$R32(h)$ (No. 155)	$P321$ (No. 150)	$P321$ (No. 150)
a (Å)	11.9901(5)	11.7867(6)	11.8898(9)	11.855(4)
c (Å)	35.553(2)	33.967(2)	9.4759(9)	9.479(5)
V (Å^3)	4426.4(3)	4086.7(3)	1160.1(2)	1153.7(8)
Z	6	6	2	2
D_{calc} (g cm^{-3})	1.494	1.619	1.369	1.376
μ (cm^{-1})	6.01	6.50	6.91	6.95
no. data collected	10952	8865	8431	7241
no. unique data	2272	2100	1784	1728
R_{int}	0.060	0.073	0.041	0.042
no. data obsd (all data)	2272	2100	1784	1728
no. variable params	135	183	125	131
R_1[a] ($I > 2\sigma(I)$)	0.072	0.057	0.061	0.051
R_w[b] (all data)	0.164	0.123	0.146	0.129

[a] $R_1 = \sum||F_o| - |F_c||/\sum|F_o|$. [b] $R_w = [\sum w(|F_o^2| - |F_c^2|)^2/\sum w|F_o^2|^2]^{1/2}$.

Table 3. Selected Bond Distances (Å), Angles (deg), and Interatomic Distances (Å) with Their Estimated Standard Deviations in Parentheses for $[Fe^{II}(H_3L)](BF_4)_2 \cdot 3H_2O$ (**1**)[a] and $[Fe^{II}(H_{1.5}L)](BF_4)_{0.5}$ (**2**)[b]

	1		**2**	
	293 K	108 K	293 K	93 K
	Bond Distances (Å)			
Fe1···N1	2.889(7)	3.523(6)	3.012(6)	3.425(6)
Fe1−N2	2.195(5)	1.989(4)	2.110(5)	2.013(3)
Fe1−N3	2.189(6)	1.981(3)	2.106(4)	1.992(3)
	Bond Angles (deg)			
N2−Fe1−N2A	103.52(16)	95.92(13)	101.60(13)	97.47(12)
N2−Fe1−N3	75.7(2)	81.08(14)	77.53(15)	81.07(12)
N2−Fe1−N3A	93.50(17)	92.20(13)	93.09(15)	91.96(13)
N2−Fe1−N3B	162.54(19)	171.61(14)	165.11(15)	170.57(13)
N3−Fe1−N3A	86.8(2)	91.17(14)	87.64(15)	89.66(13)
C1−N1−C1A	113.9(3)	119.95(3)	116.6(2)	119.88(5)
	Interatomic Distances (Å)			
O1···N4	2.790(9)	2.703(7)		
N4···N4C			2.714(8)	2.759(7)

[a] Symmetry operations for **1**: A, $-Y, X - Y, Z$; B, $-X + Y, -X, Z$. [b] Symmetry operations for **2**: A, $1 - Y, X - Y, Z$; B, $1 - X + Y, 1 - X, Z$; C, $2 - X + Y, 1 - X + Y, 1 - Z$.

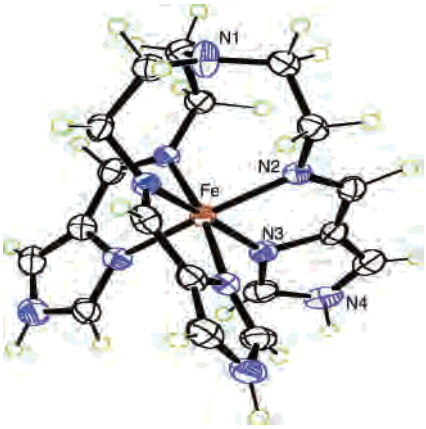

Figure 17. X-ray molecular structure of the cation of $[Fe^{II}(H_3L)](BF_4)_2 \cdot 3H_2O$ (**1**), with atom numbering scheme showing the 50% probability ellipsoids. Color code: brown, Fe; blue, N; black, C; green, H.

X-ray Structure

Structural Description of $[Fe^{II}(H_3L)](BF_4)_2 \cdot 3H_2O$ (1). Because **1** shows a gradual SCO in the 110−270 K temperature range, the X-ray crystal structure analysis was carried out at 293 and 108 K. The crystallographic data are summarized in Table 2. The same acentric space group, $R32$, is retained at both temperatures: there is no crystallographic phase transition. Selected bond lengths, angles, and hydrogen bond distances, with their estimated standard deviations in parentheses, are collated in Table 3. Figure 17 shows the ORTEP drawing of **1** at 293 K, with the atom numbering scheme showing 50% probability ellipsoids. The complex is chiral, with either a Δ (clockwise) or a Λ(anticlockwise) configuration due to the screw coordination arrangement of the achiral tripodal ligand around Fe^{II}. The complex shown in Figure 17 has the Λ configuration. Fe^{II} is surrounded by three imine nitrogen and three imidazole nitrogen atoms in an octahedral fashion. The Fe−N bond lengths at 293 K are typical for HS Fe^{II}: 2.195(5) (Fe−N(imine)) and 2.189(6) Å (Fe−N(imidazole)).[32] The corresponding values at 108 K are 1.989(4) and 1.981(3) Å. The changes in Fe−N distances by ca. 0.21 Å suggest that all Fe^{II} ions are in the LS state at 108 K.[32] This is in agreement with the magnetic susceptibility and Mössbauer results. The Fe^{II} octahedron is fairly distorted in the HS state, with *cis*-N−Fe−N bond angles in the 75.7−103.52° range. With bond angles in the 81.08−95.92° range, the octahedron is markedly less distorted in the LS than in the HS state. An increase of the Fe−N distances by ca. 0.21 Å causes such a distortion of the chelate rings that the lone pairs on the donor nitrogen atoms are not pointing directly at the metal.[33] The unit cell volume of 4426.4(3) Å^3 at 293 K decreases to 4086.7(3) Å^3 at 108 K (7.7%).

The SCO not only modifies the coordination bond lengths and angles but also the distance between N1 and Fe1 (Table 3). The nonbonding distance between N1 and Fe1 increased by ca. 0.63 Å as the temperature decreased from 293 K (2.889(7) Å) to 108 K (3.523(6) Å). The result can be explained by considering the difference in repulsion between the t_{2g} orbital electrons and the lone pair electrons of the tertiary amine nitrogen atom in the LS and HS states. The

(32) Beattie, J. K. *Adv. Inorg. Chem.* **1988**, *32*, 1−53.
(33) Reger, D. L.; Little, A.; Young, V. G., Jr.; Pink, M. *Inorg. Chem.* **2001**, *40*, 2870−2874.

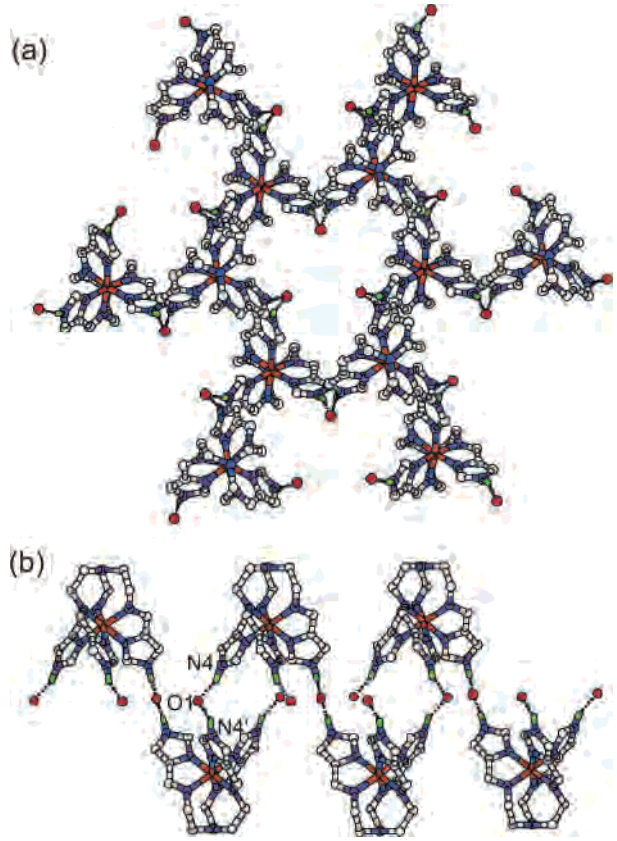

Figure 18. Crystal structure of $[Fe^{II}(H_3L)](BF_4)_2 \cdot 3H_2O$ (**1**), showing a 2D sheet formed by intermolecular hydrogen bonds through water molecules. (a) Top view. Each complex cation has a crystallographic 3-fold axis. (b) Side view. The counteranions are omitted for clarity.

tert-amine nitrogen atom (N1) is located in the center of an octahedral face and, thus, interacts more directly with t_{2g} than e_g orbitals. Four and six electrons reside in the t_{2g} orbitals in the HS and LS iron(II) states, respectively. Thus, the repulsion between the electrons in the t_{2g} orbitals and the lone pair electrons of the *tert*-amine nitrogen atom is greater in the LS t_{2g}^6 than in the HS $t_{2g}^4e_g^2$ state. Such electronic repulsion should lengthen the Fe···N(*tert*-amine) distance. At the same time, the C1−N1−C1A bond angle increased from 113.9(3)° (293 K) to 119.95(3)° (108 K). At low temperature, an almost trigonal planar geometry is observed around the *tert*-amine nitrogen atom. These results may be explained on the same grounds as above. Repulsion between the electrons in the t_{2g} orbitals and the lone pair electrons of the *tert*-amine nitrogen atom has been reported for complexes formed with the ligand $N(CH_2CH_2N{=}CHC_5H_4N)_3$.[34]

In the crystal of **1**, adjacent complex cations with the same absolute configuration are connected in a tail-to-tail fashion by N−H···O(w)···H−N hydrogen bonds, with an N···O distance of 2.790(9) Å and an N···O···N angle of 115.4(5)° at 293 K to form a puckered 2D sheet structure based on a hexanuclear unit (Figure 18, Table 3). Furthermore, the adjacent sheets with the same chirality are stacked to form a chiral crystal. These results indicate that spontaneous resolution took place during the course of crystallization. That the crystal is spontaneously resolved is demonstrated by enantiomeric circular dichroism (CD) spectra obtained from selected crystallites in KBr pellets (Figure 19). In **1**, the hydrogen bond distances associated with the uncoordinated imidazole NH groups decreased appreciably on lowering the temperature: the O1···N4 distance decreased from 2.790(9) Å at 293 K to 2.703(7) Å at 108 K. Mössbauer spectroscopy showed that, as **1** lost water of crystallization, it became SCO inactive and stayed in the HS state over the 78−298 K temperature range. The involvement of the uncoordinated imidazole NH groups in hydrogen bonds with water molecules must result in an increase in electron density on the imidazole rings, thus favoring the LS state for the metal atom. We have observed that the ligand-field strength increases upon deprotonation of $[Fe^{II}(H_3L)]^{2+}$, $[Fe^{III}(H_3L)]^{3+}$, and related complexes.[18,19] The effect of hydrogen bonds is similar to that of ligand deprotonation: it stabilizes the LS state.

(34) (a) Mealli, C.; Lingafelter, E. C. *Chem. Commun.* **1970**, 885. (b) Huheey, J. E. *Inorganic Chemistry: Principles of Structure and Reactivity*, 3rd ed.; Harper & Row: New York, 1983.

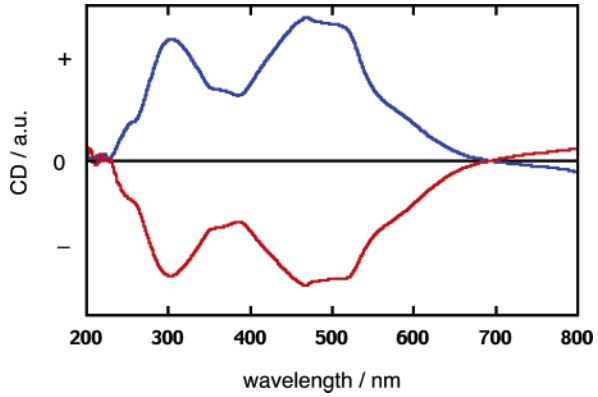

Figure 19. CD spectra of $[Fe^{II}(H_3L)](BF_4)_2 \cdot 3H_2O$ (**1**) crystallites in KBr pellets at room temperature. The two KBr pellets were prepared using selected crystals and showed enantiomeric CD patterns, providing definitive evidence for spontaneous resolution.

Structural Description of $[Fe^{II}(H_{1.5}L)](BF_4)_{0.5}$ (2). As described in the previous section, **2** was prepared several times, the samples being named **2a**−**d**. The X-ray crystal structure of **2a** was determined at 293 and 93 K, since the magnetic and ^{57}Fe Mössbauer data demonstrated that this complex exhibits SCO: **2a** is in the LS state below 200 K, and at 293 K, it is a ca. 1:1 mixture of LS Fe^{II} and HS Fe^{II}. The crystallographic data are summarized in Table 2. The same space group, *P*321, is retained at both temperatures: there is no crystallographic phase transition. The selection of the space group requires some comment. The systematic extinction of the X-ray diffraction data suggested either the *P*3 or *P*321 space group. Both structural analyses gave acceptable solutions for the space groups, *P*3 and *P*321. The unique unit in the space group, *P*3, involves two kinds of component species, whereas the unique unit in the space group, *P*321, involves only the hemi-deprotonated species $[Fe^{II}(H_{1.5}L)]^{0.5+}$.

The IR spectrum in Nujol mull showed two ν(C=N) bands at 1622 and 1594 cm^{-1}, assignable to $[Fe(H_3L)]^{2+}$ and $[Fe(L)]^-$, respectively. Moreover, in the X-ray crystal analysis of a closely related hemi-deprotonated Fe^{II} complex,

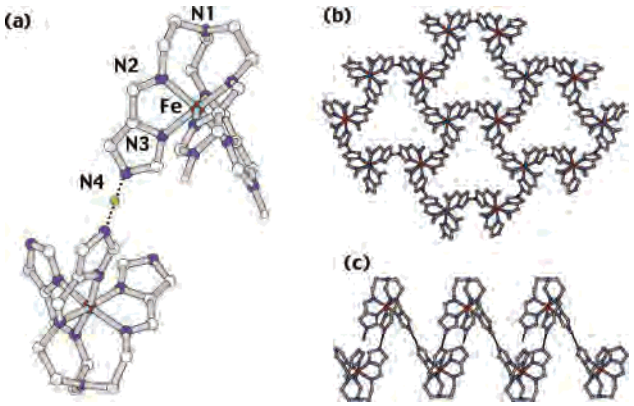

Figure 20. Crystal structure of $[Fe^{II}(H_{1.5}L)](BF_4)_{0.5}$ (**2a**). The counteranions and the hydrogen atoms, except for those attached to N4, are omitted for clarity. Color code: brown, Fe; blue, N; gray, C; green, H. (a) Crystal structure of **2a** at 293 K with the atom numbering scheme. Molecules with the same absolute configuration (Δ) are linked by imidazole−imidazolate hydrogen bonds. (b) Top view of a homochiral 2D-sheet structure formed by hydrogen bonds between the molecules. The hydrogen atoms and the counteranions are omitted for clarity. (c) Side view showing the up-and-down molecular array.

$[Fe^{II}(H_{1.5}L^{Me})](PF_6)_{0.5}$, we have shown that the complex consists of $[Fe^{II}(H_3L^{Me})]^{2+}$, $[Fe^{II}(L^{Me})]^{-}$, and PF_6^- components.[20] Thus, at first, we expected that space group *P*3 would be more appropriate. When the structure was solved assuming space group *P*3, we could not locate the hydrogen atoms of the uncoordinated imidazole NH groups of $[Fe(H_3L)]^{2+}$. Furthermore, we could scarcely distinguish between the two species; they had almost identical geometrical parameters. Although, as suggested from IR spectroscopy and X-ray crystal analysis of a related complex, **2a** should be formulated $[Fe^{II}(H_3L)][Fe^{II}(L)]BF_4$, we could not crystallographically distinguish the two sites, and thus space group *P*321 was finally selected.

Figure 20a shows the crystal structure of **2a** at 293 K with the atom numbering scheme. Selected bond lengths, angles, and hydrogen bond distances with their estimated standard deviations in parentheses are collated in Table 3. Each Fe^{II} ion is octahedrally surrounded by six nitrogen atoms. The molecule has C_3 symmetry and the tertiary amine N1 and Fe1 are located on the 3-fold axis. The molecular structure is similar to that of **1**.

The Fe−N bond lengths of **2a** at 93 K are typical of LS Fe^{II}: 2.013(3) (Fe−N(imine)) and 1.992(3) Å (Fe−N(imidazole)).[32] The corresponding values at 293 K are 2.110(5) and 2.106(4) Å, respectively. These distances are slightly shorter than the typical values for HS Fe^{II}. In general, the difference in Fe−N bond length is in the 0.14−0.24 Å range for iron(II) compounds, with $\Delta S = 2$.[2a,32] The ca. 0.11 Å change in Fe−N distances in **2a** suggests that not all Fe^{II} sites are in the HS state at 293 K, but only approximately half of them have switched from the LS to HS state. This is in agreement with the magnetic susceptibility and Mössbauer results. It is worth noting that the hydrogen bond distance increases as the temperature decreases: the N4···N4C distance increases from 2.714(8) Å (293 K) to 2.759(7) Å (93 K). This reflects the shrinking of the molecules. The associated decrease in unit cell volume from 1160.1(2) to 1153.7(8) $Å^3$ is small (0.6%).

Parts b and c of Figure 20 show top and side views, respectively, at 293 K. Component species with the same absolute configuration are linked by imidazole−imidazolate hydrogen bonds to form a 2D puckered sheet. The 2D-sheet structure is similar to fused cyclohexane rings with a chair conformation. The BF_4^- counteranion is located in the trigonal space, surrounded by the six iron components. Sheets with the same chirality are stacked to form a chiral crystal. That spontaneous resolution has been achieved is demonstrated by the enantiomeric CD spectra obtained from KBr pellets of selected crystallites (Supporting Information Figure 3).

Structural Description of $[Fe(H_{1.5}L)]BF_4$ (3). The crystal structure of **3** was determined from single-crystal X-ray analysis at 300, 220, and 100 K. These temperatures were selected on the basis of the temperature dependence of the magnetic susceptibility. The crystallographic data are summarized in Table 4, and relevant bond lengths (Å), angles (deg), and interatomic contacts (Å) with their estimated standard deviations in parentheses are listed in Table 5. The

Table 4. Crystallographic Data for $[Fe(H_{1.5}L)]BF_4$ (**3**) (=$[Fe^{II}(H_3L)][Fe^{III}(L)](BF_4)_2$)

	$C_{36}H_{45}B_2F_8Fe_2N_{20}$		
	300 K	220 K	100 K
mol wt	1043.24	1043.24	1043.24
cryst syst	trigonal	trigonal	trigonal
space group	*P*3 (No. 143)	*P*3 (No. 143)	*P*3 (No. 143)
a (Å)	11.9678(11)	11.9346(9)	11.8047(7)
c (Å)	28.5739(14)	9.4354(6)	9.3705(4)
V ($Å^3$)	3544.3(5)	1163.88(15)	1130.85(10)
Z	3	1	1
F(000)	1605	535	535
D_{calc} (Mg m^{-3})	1.466	1.488	1.532
μ(Mo Kα) (cm^{-1})	6.97	7.08	7.29
no. reflns measured	30694	9985	9692
no. unique reflns	13001	4199	4025
R(int)	0.0655	0.0532	0.0550
no. reflns obsd.[a]	9255	4034	3937
no. params refined	613	250	250
R^b (all data)	0.0430, 0.0539	0.0412, 0.0421	0.0307, 0.0311
R_w^c (all data)	0.1056, 0.1104	0.1080, 0.1089	0.0702, 0.0704

[a] Data with $F_o > 4\sigma(F_o)$. [b] $R = \sum||F_o| - |F_c||/\sum|F_o|$. [c] $R_w = [\sum w(|F_o^2| - |F_c^2|)^2/\sum w|F_o^2|^2]^{1/2}$.

Table 5. Relevant Bond Lengths (Å), Angles (deg), and Interatomic Contacts (Å) with Their Estimated Standard Deviations in Parentheses for $[Fe(H_{1.5}L)]BF_4$ (**3**) at 300, 220, and 100 K[a]

(a) $T = 300$ K

Bond Distances (Å)			
Fe1−N2	2.0130(19)	Fe4−N14	2.175(2)
Fe1−N3	1.9526(19)	Fe4−N15	2.179(2)
Fe2−N6	2.197(2)	Fe5−N18	2.093(2)
Fe2−N7	2.231(2)	Fe5−N19	2.088(2)
Fe3−N10	2.0255(19)	Fe6−N22	2.143(2)
Fe3−N11	1.9780(19)	Fe6−N23	2.142(2)
Bond Angles (deg)			
N2−Fe1−N2A	99.03(7)	N14−Fe4−N14A	105.12(6)
N2−Fe1−N3	80.82(8)	N14−Fe4−N15	75.19(8)
N2−Fe1−N3A	89.63(8)	N14−Fe4−N15A	93.99(8)
N2−Fe1−N3B	171.24(8)	N14−Fe4−N15B	159.87(8)
N3−Fe1−N3A	90.42(8)	N15−Fe4−N15A	84.69(9)
N6−Fe2−N6C	105.08(7)	N18−Fe5−N18C	101.98(7)
N6−Fe2−N7	74.60(8)	N18−Fe5−N19	76.78(9)
N6−Fe2−N7C	94.15(9)	N18−Fe5−N19C	92.37(9)
N6−Fe2−N7D	159.94(8)	N18−Fe5−N19D	165.49(9)
N7−Fe2−N7C	85.38(8)	N19−Fe5−N19C	88.78(9)
N10−Fe3−N10C	100.21(7)	N22−Fe6−N22A	103.31(7)
N10−Fe3−N11	79.68(8)	N22−Fe6−N23	75.89(9)
N10−Fe3−N11C	90.21(8)	N22−Fe6−N23A	92.81(9)
N10−Fe3−N11D	169.39(8)	N22−Fe6−N23B	163.49
N11−Fe3−N11C	89.72(8)	N23−Fe6−N23A	87.65(9)
Interatomic Distances (Å)			
N3···N7	2.788(3)	N19···N23	2.777(3)
N11···N15	2.793(3)		

(b) $T = 220$ and 100 K

	220 K	100 K
Bond Distances (Å)		
Fe1−N2	2.021(2)	1.9878(16)
Fe1−N3	2.004(2)	1.9465(17)
Fe2−N6	2.023(2)	1.9862(16)
Fe2−N7	2.007(2)	1.9502(16)
Bond Angles (deg)		
N2−Fe1−N2A	100.24(8)	98.54(6)
N2−Fe1−N3	79.67(9)	80.93(7)
N2−Fe1−N3A	90.68(9)	90.72(7)
N2−Fe1−N3B	168.88(9)	170.68(7)
N3−Fe1−N3A	89.22(8)	89.77(7)
N6−Fe2−N6A	100.16(8)	98.43(6)
N6−Fe2−N7	79.77(9)	81.05(7)
N6−Fe2−N7A	168.90(9)	170.86(7)
N6−Fe2−N7B	90.73(9)	90.67(7)
N7−Fe2−N7A	89.13(8)	89.82(7)
Interatomic Distances (Å)		
N4···N8	2.763(3)	2.748(2)

[a] Symmetry Operations: A, $1 - y, 1 + x - y, z$; B, $-x + y, 1 - x, z$; C, $1 - y, x - y, z$; D, $1 - x + y, 1 - x, z$; E, $2 - y, 1 + x - y, z$; F, $1 - x + y, 2 - x, z$.

space group is *P*3 at all temperatures. At 300 K, the structure consists of three $[Fe^{II}(H_3L)]^{2+}$ ions with the neutral ligand, three $[Fe^{III}(L)]^0$ species with the deprotonated ligand, and six BF_4^- counteranions. A plausible formulation of **3** may be $[Fe^{II}(H_3L)][Fe^{III}(L)](BF_4)_2$. The molecular structures of the component species $[Fe^{II}(H_3L)]^{2+}$ and $[Fe^{III}(L)]^0$ are similar to those of **1** and **2**. The average Fe−N bond lengths are 1.983 (Fe1), 2.214 (Fe2), 2.002 (Fe3), 2.177 (Fe4), 2.091 (Fe5), and 2.143 Å (Fe6). The values show that Fe2, Fe4, and Fe6 are HS Fe^{II}, while Fe1 and Fe3 are LS Fe^{III}, and Fe5 is HS Fe^{III}. These results on the spin state of the Fe^{II} and Fe^{III} component species are in agreement with those of the magnetic and Mössbauer studies. Adjacent $[Fe^{II}(H_3L)]^{2+}$

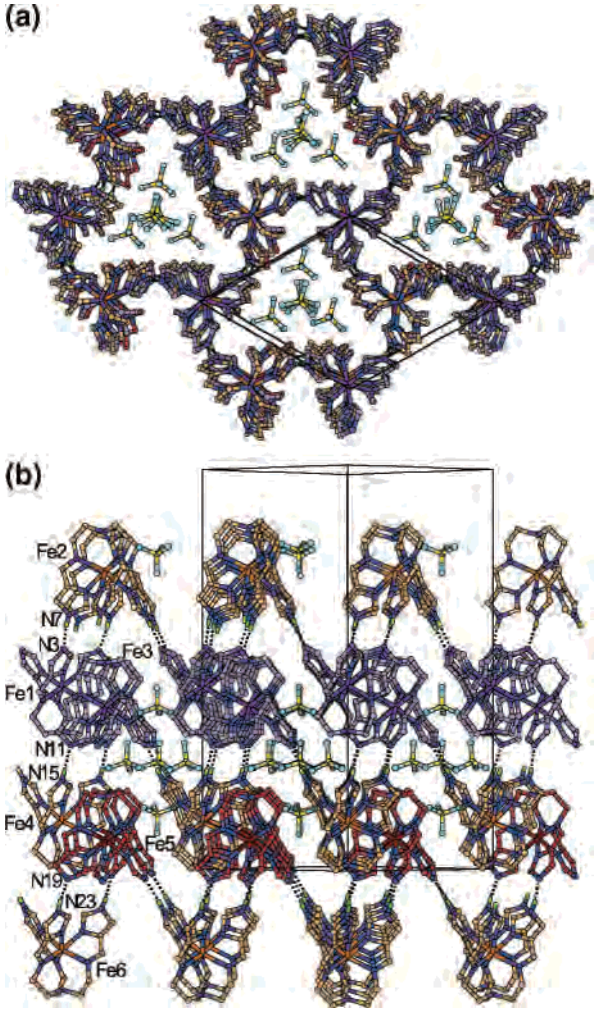

Figure 21. X-ray crystal structure of $[Fe(H_{1.5}L)]BF_4$ (**3**) (= $[Fe^{II}(H_3L)][Fe^{III}(L)](BF_4)_2$) at 300 K. Color code: orange, HS Fe^{II}; purple, LS Fe^{III}; red, HS Fe^{III}; beige, C of HS Fe^{II}; lilac, C of LS Fe^{III}; brown, C of HS Fe^{III}; blue, N; green, H; yellow, B; sky blue, F. (a) Top view showing the 2D-sheet structure, in which the same enantiomers are linked by intermolecular imidazole−imidazolate hydrogen bonds between $[Fe^{II}(H_3L)]^{2+}$ and $[Fe^{III}(L)]^0$. (b) Side view showing the stacking of sheets and the three types of layers: the first, second, and third layers consist of HS $Fe^{II}2$ and HS $Fe^{II}6$, LS $Fe^{III}1$ and LS $Fe^{III}3$, and HS $Fe^{III}5$ and HS $Fe^{II}4$ components, respectively.

and $[Fe^{III}(L)]^0$ species (Fe2 and Fe1, Fe4 and Fe3, and Fe6 and Fe5) are arrayed in an alternate up-and-down arrangement to form an extended 2D puckered-sheet structure with a hexanuclear unit (Figure 21a). The two types of component species are linked by imidazole−imidazolate hydrogen bonds. The intermolecular N···N hydrogen bond distances are in the 2.777(3)−2.793(3) Å range. A side view of the crystal structure of **3** (Figure 21b) shows that there are three types of layers: the first layer consists of HS $Fe^{II}2$ and HS $Fe^{II}6$ components, the second layer consists of LS $Fe^{III}1$ and LS $Fe^{III}3$ components, and the third layer consists of HS $Fe^{III}5$ and HS $Fe^{II}4$ components. Intermolecular hydrogen bonds connect the HS $Fe^{II}2$ to LS $Fe^{III}1$, HS $Fe^{II}4$ to LS $Fe^{III}3$, and HS $Fe^{II}6$ to HS $Fe^{III}5$ components. Each component is chiral, with either a Δ (clockwise) or Λ (anticlockwise) configuration due to the screw coordination arrangement of the achiral tripodal ligand around the Fe^{II} or Fe^{III} ion. The absolute configurations around the six iron atoms, Fe1−Fe6,

Table 6. X-ray Crystallographic Data for $[Fe^{III}(H_3L)](BF_4)_3 \cdot fim \cdot H_2O$ (**4**) and $[Fe^{III}(L)] \cdot 2.5H_2O$ (**5**)

	4		**5**
formula	$C_{22}H_{30}B_3F_{12}FeN_{12}O_2$		$C_{18}H_{26}FeN_{10}O_{2.5}$
	296 K	93 K	123 K
mol wt	810.82	810.82	478.32
cryst syst	monoclinic	monoclinic	cubic
space group	*C*2/*c* (No. 15)	*C*2/*c* (No. 15)	$I\bar{4}3d$ (No. 220)
a (Å)	38.154(2)	37.619(4)	20.175(1)
b (Å)	12.6320(4)	12.1091(9)	
c (Å)	14.1100(6)	13.995(1)	
β (°)	95.892(1)	92.480(2)	
V (Å^3)	6764.6(5)	6368(1)	8212.1(9)
Z	8	8	16
D_{calc} (g cm^{-3})	1.592	1.691	1.547
μ (cm^{-1})	5.55	5.90	7.77
no. reflns	49982	42150	29687
no. unique reflns	7620	7205	1585
R_{int}	0.024	0.045	0.049
no. reflns obsd	7281 (all data)	6873 (all data)	1585 (all data)
no. params refined	503	499	136
R_1[a] ($I > 2\sigma(I)$)	0.076	0.062	0.045
R_w[b] (all data)	0.191	0.152	0.098

[a] $R_1 = \sum||F_o| - |F_c||/\sum|F_o|$. [b] $R_w = [\sum w(|F_o^2| - |F_c^2|)^2/\sum w|F_o^2|^2]^{1/2}$.

are the same, and **3** crystallizes in the acentric space group, *P*3. These facts indicate that spontaneous resolution occurs during the course of crystallization. This is demonstrated by the enantiomeric CD spectra obtained from KBr pellets of selected crystallites (Supporting Information Figure 4).

At lower temperatures, 220 and 100 K, the *c* axis has been reduced to one-third of its 300 K length: there are only two Fe sites. At these temperatures, HS $[Fe^{II}(H_3L)]^{2+}$ and HS $[Fe^{III}(L)]^0$ have been converted to LS $[Fe^{II}(H_3L)]^{2+}$ and LS $[Fe^{III}(L)]^0$, respectively, and the structural difference between $[Fe^{II}(H_3L)]^{2+}$ and $[Fe^{III}(L)]^0$ is smaller. As a result of the SCO at $[Fe^{II}(H_3L)]^{2+}$, the satellite peaks of the X-ray reflection data disappear, and the *c* axis is reduced to one-third of its length at 300 K. As a consequence, two components of an intra-2D sheet, $[Fe^{II}(H_3L)]^{2+}$ and $[Fe^{III}(L)]^0$, as well as three Fe sites of three different layers, become indistinguishable at low temperature. This problem was discussed in detail in a previous paper.[19] The average Fe−N bond lengths are 2.013 and 1.968 Å at 220 and 100 K, respectively. Magnetic and Mössbauer studies showed that both Fe^{II} and Fe^{III} sites are in the LS state at 100 K, and the average Fe−N bond length of 1.968 Å is in agreement with these results.

Structural Description of $[Fe^{III}(H_3L)](BF_4)_3 \cdot fim \cdot H_2O$ (4) and $[Fe^{III}(L)] \cdot 2.5H_2O$ (5). The X-ray crystal structure of $[Fe^{III}(H_3L)](BF_4)_3 \cdot fim \cdot H_2O$ (**4**) was determined at 296 and 93 K.[15c] The crystallographic data are listed in Table 6, and selected bond lengths (Å), bond angles (deg), and interatomic distances with their estimated standard deviations in parentheses are listed in Table 7. Here again, the space group was retained upon cooling. The molecular structure is similar to that of **1**, and at 296 K, the average Fe−N bond distance is 2.091 Å, which is a typical value for HS Fe^{III}.[32] The corresponding distance at 93 K is 1.967 Å, which is a typical value for LS Fe^{II}. The crystal has a comblike structure (Figure 22). The complex cations are linked by intermolecular hydrogen bonds, N7−H···F1 (N7···F1 = 2.753(3) Å at 93 K), F3···H−O2 (F3···O2 = 2.750(3) Å), and O2···H−N10′ (O2···N10′ = 2.749(3) Å), to form a 1D chain running along the *c* axis. The two hydrogen bonds, N4−H···N11 (N4···N11 = 2.808(4) Å) and N12−H···F5 (N12···F5 = 2.939(3) Å), contribute to form the teeth of a comb. A similar structure has been found for the perchlorate salt.[21c]

Table 7. Selected Bond Distances (Å), Angles (deg), and Interatomic Distances (Å) with Their Estimated Standard Deviations in Parentheses for $[Fe^{III}(H_3L)](BF_4)_3 \cdot fim \cdot H_2O$ (**4**)[a]

	296 K	93 K		296 K	93 K
		Bond Distances (Å)			
Fe1−N2	2.060(3)	1.974(2)	Fe1−N6	2.112(3)	1.955(3)
Fe1−N3	2.091(3)	1.941(2)	Fe1−N8	2.078(3)	1.982(3)
Fe1−N5	2.088(3)	1.990(2)	Fe1−N9	2.118(3)	1.961(2)
		Bond Angles (deg)			
N2−Fe1−N3	76.9(1)	81.0(1)	N5−Fe1−N6	76.2(1)	81.0(1)
N2−Fe1−N5	107.1(1)	98.8(1)	N5−Fe1−N8	105.8(1)	99.4(1)
N2−Fe1−N6	88.4(1)	86.6(1)	N5−Fe1−N9	85.8(1)	85.2(1)
N2−Fe1−N8	106.0(1)	99.4(1)	N6−Fe1−N8	163.8(1)	173.9(1)
N2−Fe1−N9	165.2(1)	176.0(1)	N6−Fe1−N9	87.6(1)	93.5(1)
N3−Fe1−N5	161.5(1)	171.8(1)	N8−Fe1−N9	76.5(1)	80.5(1)
N3−Fe1−N6	85.9(1)	90.9(1)	C1−N1−C7	113.3(3)	118.8(2)
N3−Fe1−N8	89.9(1)	88.7(1)	C1−N1−C13	113.1(4)	117.7(2)
N3−Fe1−N9	88.6(1)	95.0(1)	C7−N1−C13	114.8(4)	118.9(2)
		Interatomic Distances (Å)			
F1···N7	2.785(4)	2.753(3)	O2···O2B	3.05(1)	2.937(3)
F3···O2A	2.864(9)	2.750(3)	O2···N10	2.757(9)	2.749(3)
F5···N12	2.882(9)	2.939(3)	N4···N11	2.835(5)	2.808(4)
F11···O2	3.03(1)	2.834(3)			

[a] Symmetry operations: A, *X*, 1 − *Y*, 1/2 + *Z*; B, 1/2 − *X*, 3/2 − *Y*, −*Z*.

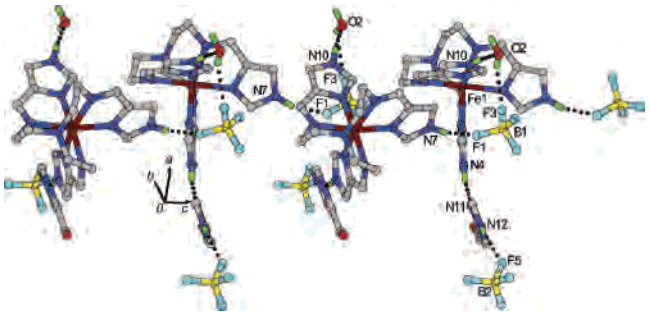

Figure 22. Crystal structure of $[Fe^{III}(H_3L)](BF_4)_3 \cdot fim \cdot H_2O$ (**4**) at 296 K, showing the comblike structure.

Table 8. Relevant Bond Lengths (Å), Angles (deg), and Interatomic Contacts (Å) with Their Estimated Standard Deviations in Parentheses for $[Fe^{III}(L)] \cdot 2.5H_2O$ (**5**) at $T = 123$ K[a]

	Bond Distances (Å)		
Fe1−N2	1.979(3)	Fe1−N3	1.917(3)
	Bond Angles (deg)		
N2−Fe1−N2A	98.1(1)	N2−Fe1−N3	80.7(1)
N2−Fe1−N3A	173.5(1)	N2−Fe1−N3B	88.3(1)
N3−Fe1−N3A	92.9(1)	C1−N1−C1A	119.0(3)
	Interatomic Distances (Å)		
O1···N4	2.70(1)	O2···N4C	2.906(9)

[a] Symmetry Operations: A, *Y*, *Z*, *X*; B, *Z*, *X*, *Y*; C, *Y* + 1/4, *X* + 1/4, *Z* + 1/4.

The X-ray crystal structure of the Fe^{III} complex, **5**, with the deprotonated ligand was determined at 123 K. The crystallographic data are listed in Table 6, and selected bond lengths (Å) and angles (deg) with their estimated standard deviations in parentheses are listed in Table 8. The molecular structure is similar to that of **1**, as shown in Supporting Information Figure 5. The average Fe−N bond distance is

1.948 Å, which is a typical value for LS Fe^{III}.[32] The oxygen atoms of the water molecules are disordered between two sites and located at a distance of ca. 2.8 Å from the noncoordinating imidazole nitrogen atom (N4).

Correlation between the CD spectral Pattern and the Absolute Configuration of Complexes 1−3. From their KBr CD spectra in the 280−800 nm range (Figure 19, Supporting Information Figures 3 and 4), we have confirmed that **1**−**3** are spontaneously resolved. All complexes exhibited a strong CD band around 320 nm, attributable to the imine $\pi-\pi^*$ transition. The structures of the complexes have been determined by X-ray crystallography. The absolute configurations of the chiral crystals, which were subjected to the X-ray analyses, were determined by the Flack parameters.[35] We have measured the CD spectra of the crystals used for the X-ray analyses. By comparing the CD spectral patterns, we conclude that complexes showing negative CD around 320 nm have the Δ absolute configuration. Very recently, we have resolved $[Co^{III}(H_2L)]^{2+}$ by fractional crystallization of the diastereomeric salt with $[Sb_2((+)\text{-tart})_2]^{2-}$ (tart = tartrate^{4-} ion) and have determined the absolute configuration by X-ray crystallography. The less soluble diastereomeric salt, $[Co^{III}(H_2L)][Sb_2((+)\text{-tart})_2]\cdot 4H_2O$, has the Λ configuration and exhibits positive CD around 320 nm.[36] Exciton theory has been applied to tris(chelate)- or *cis*-bis(chelate)-type metal complexes, where chelate denotes such ligands as 2,2′-bipyridine, 1,10-phenanthroline, or Schiff-base ligands, and the relationship between the CD pattern in the ligand $\pi-\pi^*$ transition region and the absolute configuration around the metal ion has been established.[37] The conclusions described above for the present complexes are in agreement with the assignment based on the exciton theory.

Concluding Remarks. A series of complexes, $[Fe^{II}(H_3L)](BF_4)_2\cdot 3H_2O$ (**1**), $[Fe^{II}(H_{1.5}L)](BF_4)_{0.5}$ (**2**) (=$[Fe^{II}(H_3L)][Fe^{II}(L)]BF_4$), $[Fe(H_{1.5}L)]BF_4$ (**3**) (=$[Fe^{II}(H_3L)][Fe^{III}(L)](BF_4)_2$), $[Fe^{III}(H_3L)](BF_4)_3\cdot fim\cdot H_2O$ (**4**), and $[Fe^{III}(L)]\cdot 2.5H_2O$ (**5**), has been synthesized and structurally characterized, and their properties have been extensively investigated. Although all complexes have the same FeN_6 chromophore, they offer a rich variety of SCO behaviors, which stems from cooperative intermolecular interactions. Complexes **2** and **3** are supramolecular complexes with a homochiral extended 2D structure based on imidazole−imidazolate hydrogen bonds between the components. The most remarkable structural feature of **3** is that there are three types of layers consisting of HS Fe^{II}, LS Fe^{III}, and HS Fe^{III}−HS Fe^{II} components at room temperature. The SCO behavior of **3** should be related to the supramolecular structure; in the separate $[Fe^{II}(H_3L)]^{2+}$ (**3**) and $[Fe^{III}(L)]^0$ (**5**) constituent compounds, the SCO properties are different from those in **3**. For example, **5** stays in the LS state over the 5−300 K region, while $[Fe^{III}(L)]$ in **3** switches from LS to HS above 200 K. Compounds **1**−**3** show spontaneous resolution upon crystallization. Since the complexes are photochromic, as evidenced by the LIESST experiments, these chiral compounds can be used as high-density optical data storage media with nondestructive readout, i.e., by using an optical rotation measurement. However, our compounds have CT bands in the visible region, and the change in optical activity associated with SCO should be small. Efforts are underway in our laboratories to create chiral photochromic SCO compounds without a CT band in the visible region.

Experimental Section

Materials. All reagents and solvents in the syntheses were of reagent grade, and they were used without further purification.

$[Fe^{II}(H_3L)](BF_4)_2\cdot 3H_2O$ (1). All solvents used for the synthesis of this complex contained a small amount of ascorbic acid as a reducing agent. A methanol solution (20 mL) of tris(2-aminoethyl)-amine (1.46 g, 10 mmol) was added to a suspension of 4-formylimidazole (2.88 g, 30 mmol) in methanol (30 mL). The mixture was stirred until it became clear. Then, a methanol solution (20 mL) of $FeCl_2\cdot 4H_2O$ (1.99 g, 10 mmol) was added, resulting in a rapid color change from yellow to reddish-orange. Addition of a methanol solution (30 mL) of NH_4BF_4 (3.11 g, 30 mmol) resulted in the formation of an orange precipitate. This was collected by filtration and recrystallized from ethanol. Yield 3.78 g (57%). Anal. Found: C, 32.75; H, 4.29; N, 21.12%. $C_{18}H_{30}B_2F_8FeN_{10}O_3$ = $[Fe^{II}(H_3L)](BF_4)_2\cdot 3H_2O$ requires C, 32.56; H, 4.55; N, 21.10%. IR (Nujol mull): ν(C=N_{imine}) 1639 cm^{-1}. UV−vis (MeOH): 441 nm (ϵ = 1430 M^{-1} cm^{-1}), 881 nm (ϵ = 12 M^{-1} cm^{-1}).

$[Fe^{II}(H_{1.5}L)](BF_4)_{0.5}$ (2). All procedures were carried out under an atmosphere of nitrogen, using standard Schlenk techniques to avoid oxidation. A methanol solution (100 mL) of $LiOH\cdot H_2O$ (0.021 g, 0.5 mmol) and $NaBH_4$ (0.03 g, 0.75 mmol) was added slowly to a methanol solution (80 mL) of $[Fe^{II}(H_3L)](BF_4)_2\cdot 3H_2O$ (**1**) (0.33 g, 0.5 mmol). The solution was allowed to stand overnight. The reddish-black crystals were collected by suction filtration. Yield 0.097 g. Found: C, 42.90; H, 4.75; N, 27.47%. $C_{18}H_{25.5}B_{0.5}F_2FeN_{10}O_{1.5}$ = $[Fe^{II}(H_{1.5}L)](BF_4)_{0.5}\cdot 1.5H_2O$ requires C, 42.79; H, 5.09; N, 27.72%. IR (Nujol mull): ν(C=N_{imine}) 1622, 1594 cm^{-1}. The water molecules involved in the sample seem to be adsorbed water molecules since we could not locate these water molecules in the X-ray structure analysis.

$[Fe(H_{1.5}L)]BF_4$ (3). To a warm (ca. 40 °C) methanol solution (150 mL) of $[Fe^{II}(H_3L)](BF_4)_2\cdot 3H_2O$ (**1**) (0.31 g, 0.5 mmol) was added 1 equiv of a 0.1 M aqueous NaOH solution (5 mL, 0.5 mmol). The solution was left for 1 day, and the dark green crystals that precipitated were collected by filtration and washed with a small amount of methanol. Yield 0.13 g (25%). Found: C, 41.32; H, 4.60; N, 26.70%. $C_{18}H_{22.5}BF_4FeN_{10}$ = $[Fe(H_{1.5}L)]BF_4$ = 1/2{$[Fe^{II}(H_3L)][Fe^{III}(L)](BF_4)_2$} requires C, 41.45; H, 4.35; N, 26.85%. IR (KBr disk): ν(C=N_{imine}) 1634, 1602 cm^{-1}. This complex could be prepared by using triethylamine (1.5 equiv) instead of NaOH (1.0 equiv).

$[Fe^{III}(H_3L)](BF_4)_3\cdot fim\cdot H_2O$ (4). 4-Formylimidazole (1.44 g, 15 mmol) and tris(2-aminoethyl)amine (0.73 g, 5 mmol) were mixed in water (30 mL), and the mixture was stirred at ca. 60 °C for 1 h. An aqueous solution (10 mL) of $FeCl_3$ (0.83 g, 5 mmol) was added, the resulting mixture was cooled in an ice bath, and it was stirred for 30 min. Then, an aqueous $NaBF_4$ (1.65 g, 15 mmol) solution

(35) Flack, H. D. *Acta Crystallogr., Sect. A* **1993**, *39*, 876−881.
(36) Fujii, M.; Hamada, T.; Yamaguchi, T.; Sunatsuki, Y.; Matsumoto, N.; Akashi, H.; Kojima, M. To be published.
(37) (a) Bosnich, B.; Phillip, A. T. *J. Am. Chem. Soc.* **1968**, *90*, 6352−6359. (b) Hidaka, J.; Douglas, B. E. *Inorg. Chem.* **1964**, *3*, 1180−1184. (c) Canary, J. W.; Allen, C. S. *J. Am. Chem. Soc.* **1995**, *117*, 8484−8485. (d) Zahn, S.; Canary, J. W. *Angew. Chem., Int. Ed.* **1998**, *37*, 305−308. (e) Castagnetto, J. M.; Canary, J. W. *Chem. Commun.* **1998**, 203−204.

(10 mL) was added to the mixture and stirred for another 30 min. The insoluble substance was filtered off, and the filtrate was kept in a refrigerator overnight. Dark red crystals were collected by suction filtration, washed with methanol (50 mL), and dried under reduced pressure. Yield 0.747 g (18%). Found: C, 32.83; H, 3.63; N, 20.93%. $C_{22}H_{30}B_3F_{12}FeN_{12}O_2$ = $[Fe(H_3L)](BF_4)_3 \cdot fim \cdot H_2O$ requires C, 32.59; H, 3.73; N, 20.73%. IR (KBr disk): $\nu(C{=}O_{fim})$ 1674; $\nu(C{=}N_{imine})$ 1623; $\nu(B-F)$ 1084, 1038 cm^{-1}. $\chi_M T$ = 3.88 cm^3 K mol^{-1} [5.57 μ_B] (300 K). UV−vis (MeOH): 504 nm (ϵ = 2690 M^{-1} cm^{-1}), 830 nm (ϵ = 252 M^{-1} cm^{-1}).

$[Fe^{III}(L)]\cdot 2.5H_2O$ (5). This blue complex was prepared by two methods.

Method 1. Deprotonation and Air Oxidation of $[Fe^{II}(H_3L)][B(C_6H_5)_4]_2$. To a methanol solution (20 mL) of H_3L (2 mmol) was added a methanol solution (10 mL) of $FeCl_2 \cdot 4H_2O$ (0.4 g, 2 mmol). After the mixture was stirred for 5 min, $NaB(C_6H_5)_4$ (0.58 g, 6 mmol) in methanol (10 mL) was added to yield a yellow precipitate. It was recrystallized from acetone−methanol (2:1). Yield 1.69 g (78%). Found: C, 72.99; H, 5.97; N, 13.10%. $C_{66}H_{65}B_2FeN_{10}O_{0.5}$ = $[Fe^{II}(H_3L)][B(C_6H_5)_4]_2 \cdot 0.5H_2O$ requires C, 73.14; H, 6.05; N, 12.92%.

To an acetone solution (150 mL) of $[Fe^{II}(H_3L)][B(C_6H_5)_4]_2 \cdot 0.5H_2O$ (1.1 g, 1 mmol) was added triethylamine (0.61 g, 6 mmol), and the mixture was heated at 50 °C for 1 h. The resulting blue solution was filtered, and the filtrate was concentrated to 10 mL. The blue precipitate was collected by filtration, and it was dissolved in methanol−water (5:1) and left overnight to give blue crystals. Yield: 0.22 g (46%). C, 45.32; H, 5.45; N, 29.37%. $C_{18}H_{23}FeN_{10}O_{2.5}$ = $[Fe^{III}(L)] \cdot 2.5H_2O$ requires C, 45.20; H, 5.48; N, 29.28%.

Method 2. Deprotonation of $[Fe^{III}(H_3L)]Cl_3$. 4-Formylimidazole (1.44 g, 15 mmol) and tris(2-aminoethyl)amine (0.73 g, 5 mmol) were mixed in water (30 mL), and the mixture was stirred at ca. 60 °C for 1 h. An aqueous solution (10 mL) of $FeCl_3$ (0.83 g, 5 mmol) was added to the resulting solution, and the mixture was stirred for 30 min. Addition of an aqueous solution (20 mL) of NaOH (0.602 g, 15 mmol) caused a color change from dark red to dark blue, and a dark blue powder precipitated. The powder was recrystallized from methanol−water (5:1). Yield 40%. Found: C, 45.18; H, 5.23; N, 29.22%. $C_{18}H_{23}FeN_{10}O_{2.5}$ = $[Fe^{III}(L)] \cdot 2.5H_2O$ requires C, 45.20; H, 5.48; N, 29.28%. IR (KBr disk): $\nu(C{=}N_{imine})$ 1590 cm^{-1}. UV−vis (MeOH): 551 nm (ϵ = 1160 M^{-1} cm^{-1}), 617 nm (ϵ = 1170 M^{-1} cm^{-1}).

Physical Measurements. UV−visible absorption spectra were recorded with a JASCO Ubest-550 and a Hitachi U-3410 spectrophotometer. Infrared spectra were measured on a JASCO FT/IR-550 spectrophotometer or on a Perkin-Elmer FT-IR PARAGON 1000 spectrophotometer. CD spectra were recorded with a JASCO J-720 spectropolarimeter. Cyclic voltammetry measurements were performed using a Fuso HECS 321B potential sweep unit with methanol solutions containing $LiClO_4$ (0.1 M) as supporting electrolyte. The electrochemical cell was a three-electrode system consisting of a glassy carbon working electrode, a platinum wire auxiliary electrode, and an Ag/Ag^+ (Ag/0.01 M $AgNO_3$) reference electrode. As an external standard, the Fc/Fc^+ (Fc = ferrocene) couple was observed at −0.170 V vs Ag/Ag^+ under the same conditions. The solution magnetic susceptibility measurements were carried out by the Evans method[22] on a Varian Mercury 300 spectrometer (^1H at 300 MHz) at ambient temperature (297 K). In the coaxial tube configuration, the outer 5 mm tube contained solvent (CD_3OD−2% $C(CH_3)_3OH$), while the inner tube contained a dissolved sample (ca. 0.01 M). The frequency difference between the *tert*-butyl alcohol reference signals was measured. Diamagnetic susceptibility corrections were made by using Pascal's constants. Magnetic susceptibilities of solid samples were measured with a Quantum Design MPMS SQUID magnetometer in the 5−300 K temperature range at 2 K min^{-1} sweep rate under an applied magnetic field of 1 T. Corrections for diamagnetism were applied using Pascal's constants. For the LIESST experiments, a solid-state green laser (λ = 532 nm) or a xenon arc lamp (Hamamatsu L7810) with an interference filter (Edmond Ind. Optics, central wavelength, 500 nm; fwhm, 80 nm) was used as the light source. The light was guided via an optical fiber into the SQUID magnetometer. The sample was located at the edge of the optical fiber. The measurements were performed on a very thin layer of powder sample. The weight was estimated by comparing the thermal SCO curve with that for an accurately weighed sample. The Mössbauer spectra were recorded by using a Wissel 1200 spectrometer and a proportional counter. $^{57}Co(Rh)$, moving in a constant acceleration mode, was used as the radioactive source. The hyperfine parameters were obtained by least-squares fitting to Lorentzian peaks. The isomer shifts are reported relative to metal iron foil at 293 K. The sample temperature was controlled by a Heli-tran liquid transfer refrigerator (Air Products and Chemicals, Inc.) with an accuracy of ±0.5 K. Elemental analyses were carried out on a Perkin-Elmer 2400II elemental analyzer.

X-ray Data Collection, Reduction, and Structure Determination. X-ray data of an orange crystal of **1** were obtained at 293 and 108 K using a Rigaku RAXIS-IV imaging plate area detector, using graphite monochromated Mo Kα radiation (λ = 0.71073 Å). The structure was resolved using direct methods and refined using full-matrix least-squares procedures in the CrystalStructure crystallographic software package.[38] There are two possible space groups, *R*32 (No. 155) and *R*3m (No. 160), for **1**. We solved the structure in both space groups. At both temperatures, only the space group *R*32 gave rational results. The oxygen atoms of the water molecules appeared to be disordered.

A reddish-black hexagonal plate crystal of **2**, having approximate dimensions of 0.10 mm × 0.10 mm × 0.05 mm, was mounted on a glass fiber. Measurements were made at 293 and 93 K on a Rigaku RAXIS-IV imaging plate area detector with graphite monochromated Mo Kα radiation (λ = 0.71073 Å). The data were corrected for Lorentz and polarization effects. The structures were determined by direct methods and refined on F^2 by full-matrix least-squares procedures, using the CrystalStructure crystallographic software package[38] with anisotropic displacement parameters for all non-hydrogen atoms. The hydrogen atom contributing to the imidazole−imidazolate hydrogen bond was located in the D-map but not included in the refinement at 293 K. The other hydrogen atoms were refined using the riding model. The absolute configuration was determined based on the Flack parameters.[35]

A dark red parallelepiped crystal of **3** (0.35 mm × 0.30 mm × 0.25 mm) was mounted on an Oxford-Diffraction Xcalibur diffractometer, using a graphite monochromated Mo Kα radiation (λ = 0.71073 Å) and equipped with an Oxford Instruments Cryojet cooler device. Three data collections were performed at 300 K (1), 220 K (2), and 100 K (3). The structures were determined by direct methods using SHELXS-97[39] and refined on F^2 by full-matrix least-squares using SHELXL-97[40] with anisotropic displacement param-

(38) CrystalStructure 2.00, Crystal Structure Analysis Package; Rigaku and Molecular Structure Corporation: The Woodlands, Texas, 2001.
(39) G. M. Sheldrick, *SHELXS-97. Program for Crystal Structure Solution*; University of Göttingen: Göttingen, Germany, 1990.
(40) G. M. Sheldrick, *SHELXL-97. Program for the refinement of crystal structures from diffraction data*; University of Göttingen: Göttingen, Germany, 1997.

eters for all non-hydrogen atoms. The BF_4^- anions appeared to be disordered for (2) and (3). H atoms were found on a difference Fourier map and introduced in calculations using the riding model with isotropic thermal parameters 1.1 times higher than those of the atom to which they are bonded.

A dark red prism of **4**, having approximate dimensions of 0.30 mm × 0.13 mm × 0.21 mm, was mounted on a glass fiber. Measurements were made at 296 and 93 K on a Rigaku RAXIS-IV imaging plate area detector with graphite monochromated Mo Kα radiation ($\lambda = 0.71073$ Å). Data correction and solution of the structure were carried out as for **2**. H atoms of water molecules were found on a difference Fourier map and introduced in calculations using the riding model with isotropic thermal parameters. The other H atoms were calculated and introduced in refinement using the riding model.

A deep blue prismatic crystal of **5**, having approximate dimensions of 0.20 × 0.23 × 0.21 mm, was mounted on a glass fiber. Measurements were made at 123 K on a Rigaku RAXIS−IV imaging plate area detector with graphite monochromated Mo Kα radiation ($\lambda = 0.71073$ Å). Data correction, solution of the structure, and determination of the absolute configuration were carried out as for **2**. The water molecules appeared to be disordered. Hydrogen atoms were found on a difference Fourier map and were refined isotropically.

Acknowledgment. This work was supported by a Grant-in-Aid for Science Research (grant no. 14340209) from the Ministry of Education, Culture, Sports, Science, and Technology, Japan. This work was also supported by the Mitsubishi Foundation (Mitsubishi Zaidan). The authors thank Professors Kiyohiko Nakajima (Aichi University of Education) and Makoto Handa (Shimane University) for useful discussions.

Supporting Information Available: X-ray crystallographic files in CIF format for compounds **1**−**5**, cyclic voltammograms of **1** and **5**, magnetic behavior of **2a**, CD spectra of **2** and **3** in KBr pellets, X-ray molecular structure of **5**, and tables of Mössbauer spectral parameters for **2a**, **3**, and **4**. This material is available free of charge via the Internet at http://pubs.acs.org.

IC0498384